




Alpine rockwall erosion patterns follow elevation-dependent climate trajectories

Daniel Draebing ^{1,2,3}✉, Till Mayer ^{1,3}, Benjamin Jacobs³ & Samuel T. McColl ⁴

Mountainous topography reflects an interplay between tectonic uplift, crustal strength, and climate-conditioned erosion cycles. During glaciations, glacial erosion increases bedrock relief, whereas during interglacials relief is lowered by rockwall erosion. Here, we show that paraglacial, frost cracking and permafrost processes jointly drive postglacial rockwall erosion in our research area. Field observations and modelling experiments demonstrate that all three processes are strongly conditioned by elevation. Our findings on catchment scale provide a potential multi-process explanation for the increase of rockwall erosion rates with elevation across the European Alps. As alpine basins warm during deglaciation, changing intensities and elevation-dependent interactions between periglacial and paraglacial processes result in elevational shifts in rockwall erosion patterns. Future climate warming will shift the intensity and elevation distribution of these processes, resulting in overall lower erosion rates across the Alps, but with more intensified erosion at the highest topography most sensitive to climate change.

¹Chair of Geomorphology, University of Bayreuth, Bayreuth, Germany. ²Department of Physical Geography, Utrecht University, Utrecht, The Netherlands. ³Chair of Landslide Research, Technical University of Munich, Munich, Germany. ⁴School of Agriculture and Environment, Massey University, Palmerston North, New Zealand. ✉email: d.draebing@uni-bayreuth.de

The topography of glaciated mountains reflects an interplay between tectonic uplift, crustal strength, and climate^{1,2}. During glaciations, the glacial buzzsaw^{3,4} can limit summit elevations, but glacial erosion mostly increases relief by carving deep valleys^{5,6}. During and after deglaciation, non-glacial hill-slope erosion processes, that tend to limit relief, takeover. Glacier retreat typically exposes steep, unsupported rockwalls that erode via paraglacial slope failure^{4,7,8}. Paraglacial slope failures are directly conditioned by glacial activity^{9–11}, and are prepared and triggered by glacial debuttressing^{12–14}, internal stress redistribution^{15,16} and seismic activity^{17,18} following deglaciation. Periglacial processes operate on the same rockwalls, and include frost cracking and permafrost dynamics^{3,4,7,8}. Frost cracking is a climate-driven¹⁹ mechanical weathering process that breaks down rock²⁰. Permafrost is a state of frozen ground, which can stabilise rock by increasing shear resistance²¹, but can also amplify frost cracking processes²² and cryogenic stresses, which can, along with permafrost degradation, weaken rock masses²³. These periglacial processes prime and trigger rockfalls²⁴, contributing to rockwall erosion, and have been conceptualised as a relief-limiting frost buzzsaw²⁵.

As paraglacial and periglacial processes cohabit similar topography, postglacial erosion of most alpine rockwalls is likely to be driven by a combination^{4,7,8} of glacier retreat^{26–29}, frost cracking^{30–32} and permafrost processes^{33–35}. Climate warming will modify the intensity and overlapping distribution of all three processes, and so anticipating trajectories of alpine topography evolution and rockfall hazard requires holistic quantification of these drivers. Investigation of these processes has tended to be in isolation and seldom at a landscape-scale, such that the relative contributions of these processes and their spatial distribution has hitherto never been quantified.

Here we provide a systematic analysis of postglacial rockwall erosion drivers by the integration of field and modelling experiments. We use empirically-validated models to evaluate the contributions of permafrost, frost cracking, and glacier retreat to rockwall erosion within an alpine basin. Our data indicate that paraglacial and periglacial processes combine to control climate-driven rockwall erosion in our research area and that both are elevation dependent, contributing to increased erosion rates at higher elevations. Our findings provide a potential explanation of rockwall erosion rate pattern that we compiled for the European Alps that is characterised by increasing erosion with increasing elevations. This relationship is amplified at catchments with mean rockwall elevations above 2500 m (all elevations refer to m above sea level). As these processes are linked to climate, climate warming will reduce periglacial and paraglacial erosion at lower elevations but intensify it at higher elevations. As a consequence, we propose that periglacial and paraglacial processes jointly exert a limit on postglacial summit heights, extending the existing frost buzzsaw hypothesis²⁵.

Results and discussion

Rockwall erosion in the European Alps. The most unstable alpine rockwalls exist within environments of climate extremes and climate sensitivity. An analysis of the glacier inventory³⁶ for the European Alps reveals that 85% of extant glaciers are located above 2500 m, and the majority (82.4%) are very small (<0.5 km²) (Fig. 1c). Smaller glaciers are particularly sensitive to climatic changes³⁷, so future climate warming will drive disproportionate retreat of small glaciers. Permafrost affects 6220 km² (index ≥ 0.5) of the European Alps³⁸, existing at elevations of 2200–4400 m such that most glaciers in the Alps are embedded within permafrost terrain. Consequently, high-elevation rockwalls are exposed to both paraglacial and periglacial process dynamics³⁹. To explore

the impact of these processes on erosion, we compiled rockwall erosion rates across the European Alps, which we classified into short-term (<10 a)^{40–47}, mid-term (10–2500 a)^{43,48–50} and long-term (>2500 a) rates^{31,40,51–58}. The compilation exhibits no clear spatial pattern (Fig. 1a) but reveals an increase of erosion with increasing elevation (Fig. 1b; r^2 0.46, $p < 0.001$). This relationship is stronger for areas with mean rockwall elevations above 2500 m ($r^2 = 0.64$, $p < 0.001$).

At locations with mean rockwall elevations below 2500 m, the long-term erosion rates range from $0.252^{+0.148}_{-0.142}$ mm a⁻¹ to $0.5^{+0.5}_{-0.15}$ mm a⁻¹^{40,51,52,54,55} and are higher than the short-term erosion rates of $0.05^{+0.03}_{-0.02}$ to $0.225^{+0.075}_{-0.075}$ mm a⁻¹^{40,41} from equivalent elevations. An explanation for this may be that long-term erosion rates reflect a period of more intense periglacial processes and paraglacial adjustment⁵⁹ (consistent with conceptual paraglacial exhaustion curves) that would have existed immediately following cool Last Glacial Maximum (LGM) conditions⁶⁰. Long-term erosion rates may also integrate a period of elevated post-glacial seismic activity, suggested to have increased mass movements in some locations¹⁸. In contrast, the short-term rates below 2500 m represent areas that are presently glacier- and permafrost-free and with relatively mild frost cracking³².

For rockwall elevations above 2500 m, which are potentially affected by permafrost (Fig. 1c), long-term erosion rates range from $0.252^{+0.148}_{-0.142}$ to $3.2^{+1.3}_{-1.8}$ mm a⁻¹^{31,51–53,56–58}, and mid-term rates are between $0.83^{+0.629}_{-0.416}$ and 2.9 mm a⁻¹^{43,48,50}. The short-term erosion rates are generally greater, ranging from $0.4^{+0.3}_{-0.3}$ to 14.4 mm a⁻¹^{41–47}. The greatest erosion rates are from glacier headwalls, ranging from $1.9^{+8.40}_{-1.55}$ to 8.4 mm a⁻¹^{44–46}, or high-elevation permafrost-affected rockwalls with rates of up to 14.4 mm a⁻¹⁴³. More intense modern erosion rates at high elevations, compared to low elevations, have previously been hypothesised to reflect permafrost degradation and active-layer thaw^{43,45,46} or increased frost weathering within bergschrunds⁴⁷, but such hypotheses have not been robustly tested and have tended to ignore paraglacial effects.

The time-scale dependant contrast in erosion rates above and below 2500 m suggests that elevation, though its influence on local climate, is a fundamental control on erosion processes. The patterns we observe are unlikely due to data preservation bias or the Sadler effect⁶¹ (like has previously been observed in glaciated landscapes with short term rates exceeding long-term rates, interpreted as bias⁶²). The data we compiled reveal no consistent pattern of short-term erosion rates being greater than long-term rates (Fig. 1d), with instead long-term rates exceeding short-term rates at lower elevations. Sedimentary incompleteness can introduce bias⁶¹, but the long-term rockwall erosion rate data are largely from coarse-grained sedimentary archives such as talus slopes^{40,49–54,58} or rock glaciers^{48,57} that are unlikely to have major sediment depletion gaps. There is limited opportunity for reworking and erosion of such coarse-grained deposits, which are located mostly within low-connectivity systems, such as disconnected glacial hanging valleys, and are net stores of postglacial sediment⁶³. Furthermore, as our data compilation is from a single orogen we can exclude bias arising from comparing sites that experience markedly different tectonic regimes. In the following section, we evaluate the hypothesis that elevation is a first-order control on rockwall erosion rate patterns through its influence on periglacial and paraglacial processes.

Rockfall processes and potential influencing factors. To explore the relationship between elevation and rockwall erosion rate for the European Alps, we quantified and modelled periglacial and paraglacial processes and compared these to patterns of

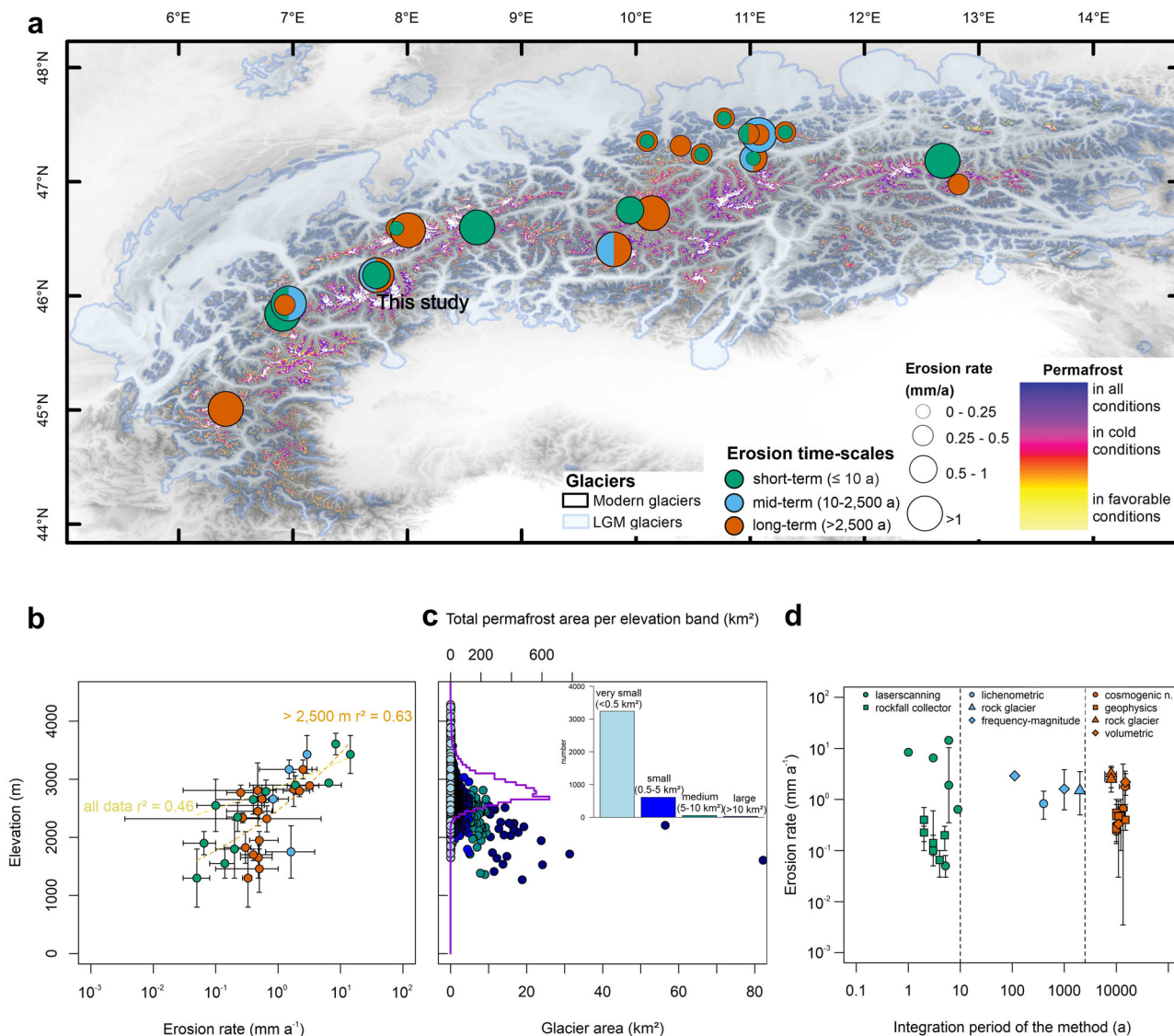


Fig. 1 Rockwall erosion rates along glacier and permafrost distribution in the European Alps. **a** Compiled short-term, mid-term and long-term erosion rates in the European Alps along with the extent of LGM glaciation¹⁴⁴, current glaciers³⁶ and permafrost distribution^{38,114} (DEM source: European Digital Elevation Model). **b** Relationship between erosion rates and elevation. The linear relationship increases from $r^2=0.46$ for all erosion rates to $r^2=0.63$ ($p < 0.001$) when limited to catchment areas with mean elevation >2500 m. **c** Inset histogram: frequency of very small glaciers (<0.5 km², light blue), small glaciers (0.5 to 5 km², blue), medium-sized glaciers (5 to 10 km², turquoise) and large glaciers (>10 km², dark blue) in the Alps. Main graph: Elevation of the terminus³⁶ of different sized glaciers (using same colours as for inset histogram) and permafrost distribution (purple line)^{38,114}. **d** Comparison of short-, mid- and long-term erosion rates, to evaluate influence of integration period (i.e. time-scale) on calculated erosion rates. Error bars indicate the minimum and maximum range of rockwall elevation and erosion rates. For detailed erosion rates including used methods, see Supplementary Table 1.

contemporary and post-LGM rockfall activity in an alpine valley. We chose the Hungerli Valley (Fig. 2), a hanging valley of the Turtmann Valley, itself a tributary of the Rhône Valley, Valais, in the southern Swiss Alps. The Hungerli Valley hosts a very small (0.045 km² in 2017⁶⁴) cirque glacier (Rothorn Glacier), steep rockwalls, and sedimentary landforms (moraine, rock glaciers⁶⁵ and talus slopes⁶³) disconnected from the Turtmann Valley⁶³ (Supplementary Fig. 1). The rockwalls have been glacially eroded and experienced phases of glacial advance and retreat since the LGM. With periglacial conditions and a glacier terminus above 2850 m, the Hungerli Valley is representative of many alpine valleys in the European Alps (Fig. 1c). The rockwalls studied occur on the north and north-east facing slopes of Hungerlihorli peak and Rothorn cirque, respectively, with elevations from 2500 to 3277 m.

We detected 263 rockfall events in the valley between 2016 and 2019 using annually repeated terrestrial laser scanning. Rockfall volumes ranged from 0.1 to 159.4 m³ (Fig. 3a), with a median of 0.26 m³, and 96% being smaller than 10 m³ (Fig. 4e). The rockfall magnitude-frequency data exhibit a typical inverse relationship ($N_{2016-19} = 17.59 V^{-0.68}$; Fig. 3a), with a power law exponent, within the range (-0.48 to -0.77) of those previously published for alpine rockwalls^{40,43,47,66}, that differs little between the three years ($N_{2016-17} = 19.08 V^{-0.57}$, $N_{2017-18} = 17.97 V^{-0.76}$, $N_{2018-19} = 18.01 V^{-0.65}$). Studied rockwalls possess a modal elevation of 2900–3000 m (using 100 m elevation bands; Fig. 4a). The median rockfall volume scales positively with increasing elevation below the 3000–3100 m elevation band and negatively above this band (Fig. 4e), rather than following the distribution of available rockwall area proportionally (Fig. 4a). Most high-magnitude (> 10 m³)

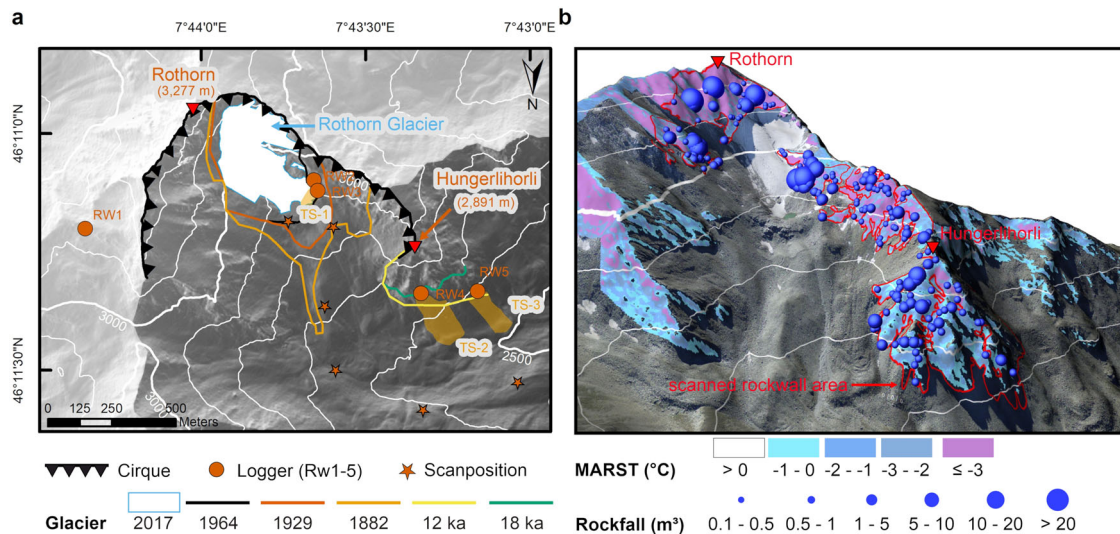


Fig. 2 Rockfall events along with glacier history, permafrost distribution and talus slopes in the Hungerli Valley. **a** Scanned rockwalls of the Hungerli Valley with highlighted glacier history (coloured lines). Instrumented rockwalls (red point), investigated talus slopes (brown polygons) and scan positions (red stars) are highlighted (source: swissALTI3d from swissTopo). **b** 3D representation of scanned rockwall area (red rectangle), modelled permafrost distribution and quantified rockfall volumes for 2016 to 2019 (source: swissALTI3d and swissIMAGE25 from swissTopo).

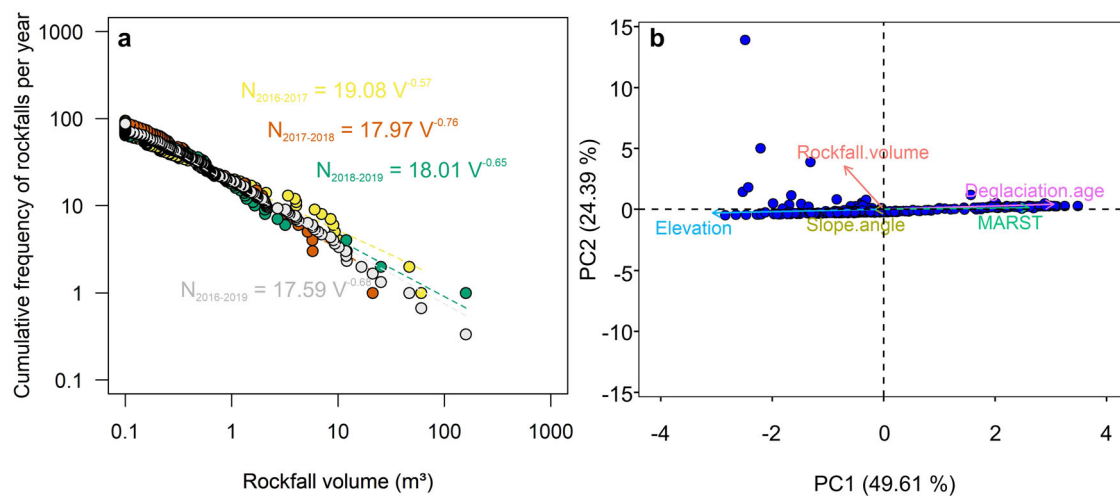


Fig. 3 Rockfall events and statistical analysis of controlling factors. **a** Rockfall frequency-magnitude distribution for individual periods (2016-17 in yellow, 2017-18 in red, 2018-19 in green) and for the entire 2016-2019 period (in grey) in the Hungerli Valley. Linear correlation r^2 of power laws is between 0.98 and 0.99 with $p < 0.001$. **b** PCA of rockfall variance between five variables: deglaciation age (i.e. proxy for paraglacial condition, elevation (proxy for frost cracking), MARST (proxy for permafrost), slope angle, and rockfall volume.

events occurred between 2900 and 3200 m, which encompasses most of the elevation range of the present-day glacier (Fig. 2).

As a preliminary exploration of rockfall patterns in the Hungerli Valley, we used a principal component analysis (PCA) to examine statistical relationships between modelled or inferred periglacial and paraglacial conditions, and topography. For each rockfall we related the deglaciation age (i.e. a paraglacial proxy; from historical aerial photos, moraine positions, and ice surface reconstructions), mean annual rock surface temperature (MARST; from a rock surface temperature driven permafrost model⁶⁷), elevation (i.e. a frost cracking proxy), slope angle (i.e. shear stress proxy), and the rockfall volume. The results show that the first two PCA dimensions explain 74.0% of the data variation (Fig. 3b), with a strong relationship found for deglaciation age (Eigenvalue 0.84) and MARST (0.72), and an inverse relationship with elevation (-0.85) on dimension 1 (PC1). The results suggest that all three elevation-dependent

processes (deglaciation history, permafrost, and frost cracking) correlate, and are therefore potentially involved in explaining the modern rockfall activity at Hungerli Valley. The slope angle of the rockfall (low eigenvalue of -0.04) has low correlation to the other variables. We suggest this is due to the steep nature of the rockwalls, such that threshold slope conditions and sensitivity to triggers exist over much of the rockwall^{68,69}. Consequently, at the scale of individual rockwalls, the external drivers (paraglacial stress release and debuitting, and periglacial processes), all of which are elevation dependent, may be more important than slope form (i.e. slope oversteepening from glacial erosion) at explaining the local distribution of rockfall^{5,70,71}. Rockfall volume (-0.20) relates to PC2. Rockfall volume is likely to be influenced by differences in the fractures spacings and patterns of the rock masses present in the valley, which while not explicitly included in the PCA, are captured by variation in elevation and possibly slope angle.

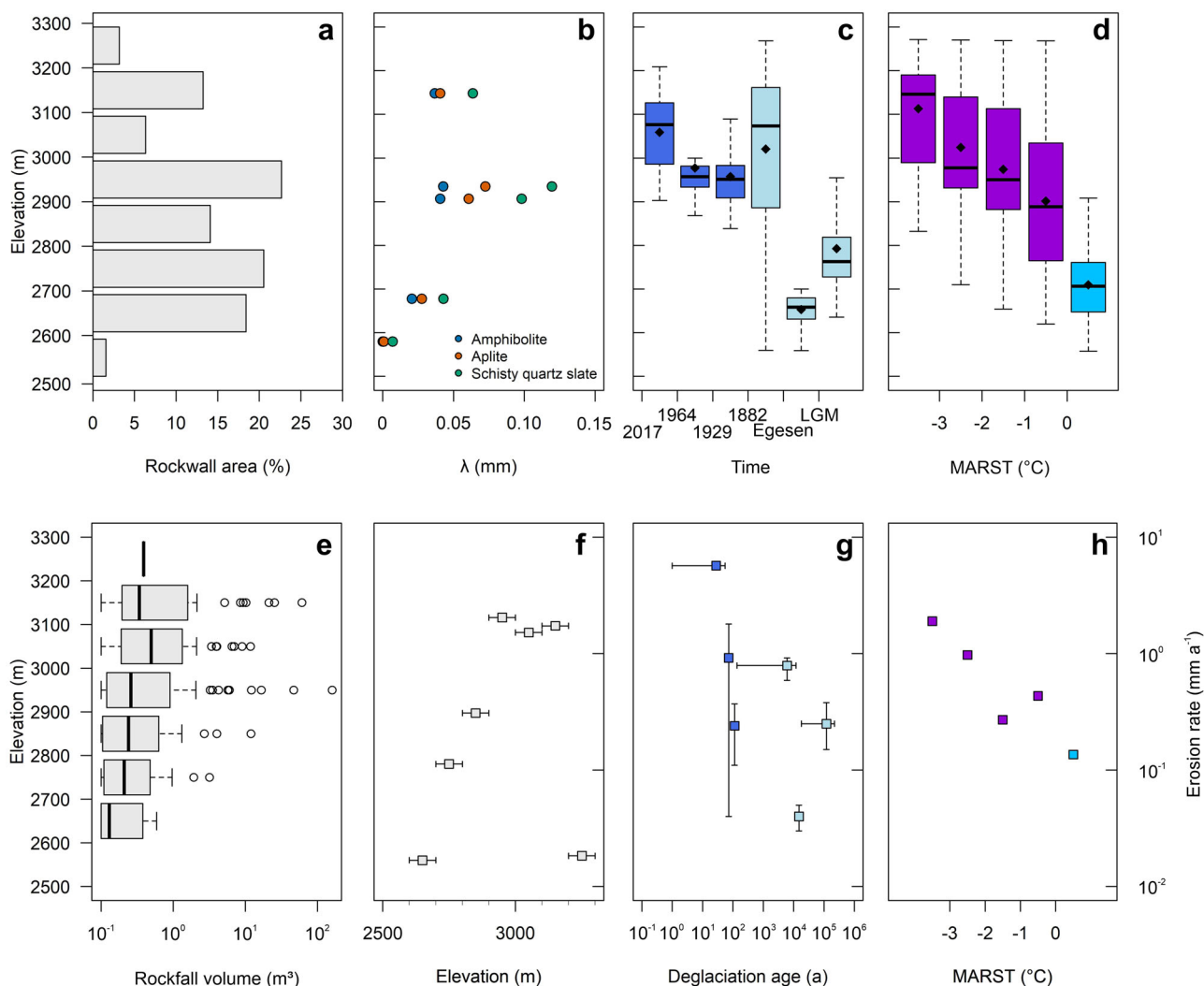


Fig. 4 Factors influencing rockwall erosion rates and their variation along elevation. **a** Rockwall area distribution per 100 m elevation band. The presence of scree and glacial cover reduces the area of exposed rockwall within the 2800–2900 m and 3000–3100 m elevation bands (Fig. 2). **b** Modelled frost cracking intensities for different rock types, plotted against elevation. For detailed mean and annual frost cracking, see Supplementary Fig. 7. **c** The elevation distributions of newly deglaciated areas from the LGM to 2017 with mean elevation as diamonds. **d** MARST plotted against elevation; permafrost is shown in violet and permafrost-free areas are light blue with mean elevation as diamonds. **e** Rockfall volumes at different elevation bands with solid bars indicating median values and points are statistical outliers. Short-term erosion rates plotted against (f) elevation, (g) deglaciation age and (h) MARST. Error bars indicate the minimum and maximum range of rockwall elevation or erosion rate. Colours in g and h refer to applied colour schemes in c and d.

Spatial distribution of rockfall driving processes. Here we refine and analyse the spatial distribution of the three most correlated PCA variables; frost cracking, MARST (permafrost) and deglaciation age (paraglacial adjustment). Whereas for the PCA we treated elevation as a proxy for frost cracking, here we modelled frost cracking by applying a thermo-mechanical model⁷² to measured rock surface temperatures³². Modelled frost cracking affects all rockwall locations in the Hungerli Valley, but is most intense within the three highest permafrost-affected rockwalls (RW1-3; Supplementary Fig. 5), and varies by rock type/strength within each elevation band (Supplementary Fig. 7). Rock type ranges from weaker schisty quartz slate with aplite inclusions in the Rothorn cirque to stronger schisty quartz slate with inclusions of amphibolite and aplite in the Hungerlihorli (Supplementary Figs. 1 and 2)⁷³. Regardless of the influence of lithological variations (Fig. 4b), a strong (non-monotonic) relationship was persistent between frost cracking and elevation. Our model results suggest frost cracking increases with elevation up until 3000 m, thereafter reducing at higher elevations (Fig. 4b). The modelled

penetration depth of frost cracking is mostly shallower than 0.5 to 2 m, and exhibits increasing depth at higher elevations, up until ~3000 m (Supplementary Fig. 6). The modelled frost cracking pattern corresponds to the measured fracture spacing³², with more intense frost cracking generating more near-surface fracturing. As potential rockfall size is limited by the spacing of fractures, areas of more intense frost cracking will likely produce more numerous but smaller rockfalls, and be unlikely to trigger large events (>10 m³).

Modelled MARST (a proxy for permafrost) is inversely related to elevation in the Hungerli Valley (Fig. 4d), such that colder MARST and permafrost likelihood increase at higher elevations. Rockwall with MARST below -3°C is located at a mean elevation of 3113 m (1st Q. = 2989 m; 3rd Q. = 3190 m), whereas rockwall with MARST between -1 to 0°C is located at a mean of 2901 m (1st Q. = 2765 m; 3rd Q. = 3034 m) (Fig. 2d). Permafrost-free areas (taken to have positive MARST) exist mostly below 2760 m, whereas above 2800 m, 75% of the rockwall area is frozen, and above 3100 m nearly the entire rockwall is affected by

permafrost (Fig. 2). While MARST provides an indication of permafrost presence^{66,74}, it cannot be used to assess the depth of seasonal warming and thaw, which influence rockfalls by decreasing shear resistance^{21,75–77} or increasing hydrostatic pressure²¹. The depth of warming and thaw depend additionally on seasonal temperature fluctuations and insulating snow cover⁷⁸, which are challenging to model at a landscape scale. Consequently, we use MARST only as a proxy for permafrost presence, which we in turn use to identify rockwalls that are likely to have permafrost-related instability processes present (without modelling the processes themselves).

The deglaciation history since the LGM has resulted in a general trend for newly exposed rockwalls to occur at higher elevations over time (Fig. 4c). The general trend deviates because glacier retreat can involve thinning (vertical retreat) and terminus recession (planform retreat), both of which expose new rockwall but at different elevations (as evidenced by historic photos; Supplementary Fig. 3 and Fig. 2a). Between the LGM and Egesen, the thickness of the valley glacier decreased, and newly-exposed rockwalls (mean = 2653 m; 1st Q. = 2631 m; 3rd Q. = 2680 m; Fig. 4c) were restricted to the Hungerlihorli (Fig. 2). Between the Egesen and Little Ice Age (LIA), retreat of the valley glacier involved thinning and lateral retreat of the Rothorn cirque glacier, exposing new rockwall across a large elevation range (1st Q. = 2886 m; 3rd Q. = 3162 m; Fig. 4c). Since the 19th century (i.e. LIA), new rockwall exposure in Hungerli Valley has been occurring generally at higher elevations over time (Fig. 4c); between 1882 and 1929 the mean elevation of newly exposed rockwall was 2958 m (1st Q. = 2909 m; 3rd Q. = 2982 m), which increased to 3059 m (1st Q. = 2986 m; 3rd Q. = 3127 m) between 1964 and 2019. For context, the present-day Rothorn Glacier is located between 2850 and 3100 m (Fig. 2a).

Short-term rockwall erosion rates. To quantify short-term rockwall erosion in the Hungerli Valley, we converted our contemporary rockfall data (volumes, m³) into annual rockwall erosion rates (mm a⁻¹) by dividing by the area of scanned rockwall. We then explored how erosion rate varies with the patterns of frost cracking, permafrost and paraglacial processes described above. The mean rockwall erosion rate of the entire scanned area was 0.86 mm a⁻¹ between 2016 and 2019, but varies with elevation (assessed for 100 m elevation bands; Fig. 4f). Between 2600 and 3000 m the mean rockwall erosion rates increased with elevation, from 0.02 mm a⁻¹ at the 2600–2700 m elevation band to 2.04 mm a⁻¹ at the 2900–3000 m band. At higher elevations, the rates became smaller (1.52 mm a⁻¹ at 3000–3100 m; 1.73 mm a⁻¹ at 3100–3200 m, and 0.02 mm a⁻¹ above 3200 m). The elevation bands with the greatest erosion rates, between 2900 and 3200 m (Fig. 4f), correspond to elevations with the most intense frost cracking (Fig. 4b). While frost-cracking rates are known to vary with elevation^{32,72,79}, hitherto frost-cracking rates had not been quantitatively and directly linked to rockwall erosion rates. Previous research suggested that frost cracking is positively related to catchment-wide erosion but inversely related to elevation⁸⁰. This contrasts with our observed positive relationship between rockwall erosion rates and elevation. Catchment-wide erosion rates are measured from stream sediments that integrate multiple erosion processes throughout a catchment⁸¹. Moreover, rockwall erosion products (i.e. coarse rockfall debris) tend to be stored (e.g. in talus) with poor downstream connectivity. Consequently, and especially because rockwalls are underrepresented according to hypsometric curves^{3,7}, the contribution of rockwall erosion to catchment-wide erosion and the relationships between rockwall erosion and its drivers are poorly captured by catchment-wide erosion rate measurement approaches.

Rockwall erosion rates in the Hungerli Valley also vary with deglaciation age, generally increasing from the oldest to the most recently deglaciated rockwalls. Ice-free rockwalls (on the Hungerlihorli) and rockwalls deglaciated between the LGM and Egesen had erosion rates of $0.25^{+0.14}_{-0.10}$ and $0.04^{+0.01}_{-0.01}$ mm a⁻¹, respectively. Allowing for the possibility of a cold-based glacier occupying the Hungerlihorli (i.e. reducing the area of exposed rockwall) between LGM and Egesen, the erosion rate increases to $0.13^{+0.06}_{-0.06}$ mm a⁻¹. Between the Egesen and 1882, a large part of the cirque became glacier-free and 30% of all recorded rockfalls, including the largest (159 m³), occurred within this area. These rockfalls contributed to an erosion rate of $0.79^{+0.13}_{-0.20}$ mm a⁻¹. For rockwalls deglaciated between 1882 and 1929 there was an erosion rate of $0.24^{+0.13}_{-0.13}$ mm a⁻¹, which increases to a rate of $0.92^{+0.88}_{-0.88}$ mm a⁻¹ for those deglaciated between 1929 and 1964. The greatest rate, of $5.69^{+0.44}_{-0.44}$ mm a⁻¹, was for rockwalls deglaciated between 1964 and 2019 (Fig. 4g). In general, rockfalls were prevalent in proximity to the extant glacier, with 77 rockfalls or 29% of all measured events, including four >10 m³ sourced from rockwalls deglaciated between 1964 and 2019. Enhanced rockfall erosion in proximity to a retreating cirque glacier margin has been observed elsewhere⁴⁴ for which paraglacial processes such as thermo-mechanical stresses¹³, unloading stresses amplified by cirque glacier erosion^{12,82}, or increased frost cracking within a bergschrund⁸³ may play a role. While we do not know which processes operate at the Hungerli Valley, the rockwall erosion rate patterns, at least partly, appear to reflect paraglacial adjustment^{9,84}. Moreover, while some studies have suggested paraglacial rockwall adjustment (i.e. stress release and fracture propagation) operates at a millennial timescale^{12,15}, our data show that adjustment can be more rapid (i.e. over decadal timescales). The older rockwalls in the Hungerli Valley may still be experiencing gradual paraglacial adjustment, but the rates of adjustment have slowed over time, as predicted by paraglacial exhaustion curves^{9,84}.

We also find a relationship between modelled permafrost and rockfall erosion rates. Permafrost-affected rockwalls revealed higher erosion rates ranging from $0.27^{+0.01}_{-0.01}$ to $1.90^{+0.04}_{-0.04}$ mm a⁻¹ than permafrost-free rockwalls ($0.14^{+0.00}_{-0.01}$ mm a⁻¹; Fig. 4h). Erosion rates decrease with increasing MARST. While MARST gives information about potential presence of permafrost, it does not reflect the magnitude of active-layer thaw^{21,85} or cryostatic pressures from refreezing²³, which drive rockfall generation. However, 92% of all rockfall events (and 97% by volume) were released from permafrost-affected rockwalls, producing an overall erosion rate of $1.01^{+0.02}_{-0.02}$ mm a⁻¹, suggesting the importance of permafrost presence in rockwall erosion.

Long-term rockwall erosion rates. To evaluate rockwall erosion rates within a longer temporal framework, we used geophysics to measure the volume of three talus accumulations in the Hungerli Valley. Talus slope-1 (TS1)—within the cirque and below a rockwall source area with elevation of 2900–3000 m (Fig. 2a)—integrates 55 years of rockfall accumulation, giving a rate of $50.7^{+10.9}_{-10.3}$ mm a⁻¹. This erosion rate is one order of magnitude higher than those measured using the contemporary (i.e. 2016–2019) rockfall data from the same (2900–3000 m) elevation band (2.04 mm a⁻¹; Figs. 4f and 5f) or from rockwalls of equal deglaciation age ($5.69^{+0.44}_{-0.44}$ mm a⁻¹; Fig. 4g).

Talus slope-2 (TS2) and Talus slope-3 (TS3) are located at the base of Hungerlihorli peak, an area last glacierized during the Egesen stage (Younger Dryas), and integrate 10 to 12 ka of rockfall activity. The contributing rockwalls are located between 2600 and 2891 m for TS3 and between 2620 and 2891 m for TS2, and their talus

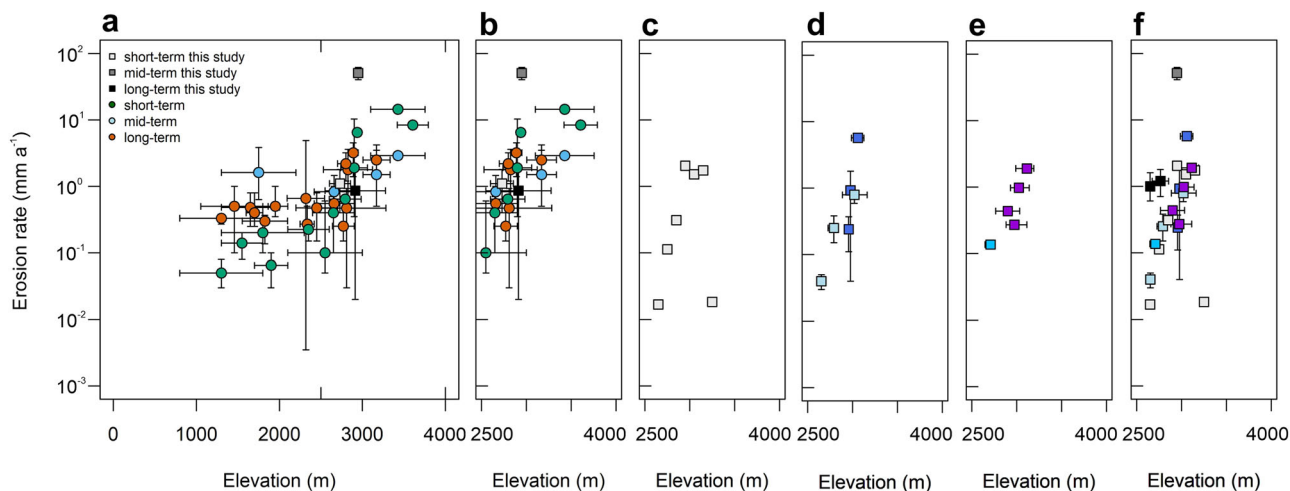


Fig. 5 Erosion rates increase with increasing elevation. **a** Compiled mean short-term, mid-term and long-term erosion rates from the European Alps, complemented by short-term, mid-term and long-term erosion rates from the Hungerli Valley. Error bars indicate the range in elevation and erosion rate. **b** The same data as plot (a), but for elevations of 2500 m and above only. **c** Short-term erosion rates only, for the Hungerli Valley. **d** Mean short-term erosion rates of the Hungerli Valley versus the mean elevation of each deglaciation age class. Error bars show range of erosion rates and 1st and 3rd quartile of elevation of deglaciation age class (see Fig. 4c). **e** Short-term erosion rates of the Hungerli Valley versus mean elevation of MARST class. Error bars show 1st and 3rd quartile of elevation of MARST class (see Fig. 4d). **f** Data from plots (c–e) plotted together with mid-term and long-term erosion rates determined from talus slopes. For colour scheme of (c–f) see Fig. 4.

accumulations suggest rockwall erosion rates of $1.0^{+0.6}_{-0.4}$ mm a⁻¹ (TS3) to $1.2^{+0.6}_{-0.5}$ mm a⁻¹ (TS2). The erosion rates are one to two orders of magnitude higher than those measured using the contemporary rockfall (i.e. laser scanning) data from the equivalent elevation bands (0.02 to 0.31 mm a⁻¹; Figs. 4f and 5f). It is probable that the rates from long-term measurements exceed those of the short-term measurements due to integrating an aggressive period of paraglacial adjustment (expected soon after glacier retreat), and more intense permafrost thaw and frost cracking during colder phases (e.g. LIA) of the Holocene. The long-term measurements possibly also integrate episodic co-seismic rockfall activity, with more than 36 M_w 4.0 and larger events recorded in Switzerland since 250 AD⁸⁶ and possibly increased seismic activity following deglaciation like found elsewhere^{17,18}.

Elevation-dependent paraglacial and periglacial processes and their implications for rockwall erosion patterns in the European Alps.

The short-term and long-term erosion rates in the Hungerli Valley both share the same positive relationship between elevation and erosion rates that was found for data compiled for the entire European Alps (Fig. 5a), especially at elevations above 2500 m (Fig. 5b). Our analyses from the Hungerli Valley suggest that this relationship is driven by frost cracking, permafrost occurrence and deglaciation age, all of which vary with elevation. Our modelled frost cracking magnitudes are elevation-dependent (Fig. 4b) and correspond to erosion rates increasing with elevation (Fig. 5c) up until a threshold elevation. Above this threshold, frost cracking decreases with increasing elevation^{72,79} due to a decreasing availability of water (essential for frost cracking) at higher elevations^{72,87}. This decreasing pattern is reflected in our frost cracking results, with reduced frost cracking at 3150 m (Fig. 4b), but the decrease will be more apparent for rockwalls that reach elevations higher than those of the Hungerli Valley. It is likely that frost cracking will be relatively minor on the highest summits of the Alps in the present climate, but will increase with further warming.

When we substitute elevation for MARST (i.e. permafrost), we see that permafrost presence contributes to greater erosion rates at

higher elevations at our research area (Fig. 5e). Based on the European Alps permafrost model, most rockwalls above ~2800 m are potentially affected by permafrost³⁸, and therefore are likely to be experiencing elevated rockwall erosion rates, as presumed by previous high-elevation studies^{41–43,45,46}. The development of regional scale models that can quantify the magnitude of active-layer thaw and permafrost warming effects (in addition to permafrost presence) will help to further evaluate the patterns we observe.

Substituting elevation for deglaciation age (Fig. 4c) reveals that short-term erosion rates increase with elevation in the Hungerli Valley (Fig. 5d), suggesting an elevation dependency to paraglacial adjustment. Over 80% of glaciers in the Alps are very small and located above 2500 m. These glaciers are very sensitive to climatic changes³⁷ and are retreating rapidly (in length but also laterally, especially within cirques), as observed for the Rothorn Glacier (Fig. 2). Consequently, our catchment scale study suggests that paraglacial processes will be responsible for a short-term increase (i.e. rapid adjustment) in rockwall erosion, especially at elevations above 2500 m.

Permafrost, frost cracking, and glacier retreat do not operate in isolation, but overlap and interact. Like for most alpine valleys, rockwalls deglaciated since the LIA in our research area (Fig. 4c) are located at elevations with permafrost (Fig. 4d). When warm-based glaciers retreat within permafrost terrain, rockwalls lose the insulating effect of the ice^{88,89}, allowing permafrost to encroach into the newly exposed rockwall⁸⁹, potentially increasing rockwall erosion²³ until the climate has sufficiently warmed to degrade all permafrost at those elevations. In a similar way, glacier retreat can introduce new thermo-mechanical stresses by exposing rockwalls to ambient temperature fluctuations¹³. Glacier retreat can also expose large bedrock fractures lengthened by glacier stresses^{12,14,15}. As frost cracking is sensitive to crack length^{32,72,87} and larger cracks freeze first⁹⁰, the exposure of large cracks can facilitate more efficient frost cracking³². Permafrost presence can also amplify frost cracking, through bidirectional freezing²², which produces the highest rates in frost cracking models³². As a consequence of these interactions, climate warming has a profound, but non-uniform, effect on the breakdown of rockwalls by shifting the distribution and intensity of multiple paraglacial and periglacial processes.

Climate warming in the European Alps is causing the retreat, and eventual disappearance, of very small glaciers³⁷, which will drive paraglacial rockwall adjustment and the temporary growth—but long-term warming and degradation—of permafrost³³. That warming and retreat will intensify frost cracking at higher elevations and in proximity to retreating glaciers, respectively, whereas at lower elevations the warming will reduce frost cracking³². Although lower elevations will experience a reduction of periglacial and paraglacial processes, other climate-dependent weathering processes¹⁹ such as chemical and thermal weathering^{91–93} may replace them as the main drivers of rockwall erosion⁹⁴. Over time, the areas of most intense periglacial and paraglacial processes and resulting erosion will shift to higher elevations, in locations where higher topography exists.

Methods

Rockwall erosion rates in the European Alps. We compiled existing rockwall erosion rate data for the European Alps (Supplementary Table 1) and classified them into short-term (≤ 10 years), mid-term (> 10 to ≤ 2500 years) and long-term (> 2500 years) erosion rates. Short-term erosion rates were derived from rockfall collectors⁴¹ or terrestrial laserscanning campaigns^{40,42,43,45–47} and integrate several years of rockfall activity (Fig. 1d). Due to the short integration time, these erosion rates are unlikely to include low-frequency high-magnitude events; however, if they do then the rates can be grossly over-estimated. Mid-term erosion rates (integrating 10 to 2500 years) were derived from lichenometric measurements⁵⁰, averaged rates from talus-derived rock glacier deposits⁴⁸ or up-scaled rates using rockfall frequency-magnitude relationships^{43,49}. Long-term rockwall erosion rates (integrating > 2500 years) were provided from geophysical imaging^{51–54} or morphological estimation^{40,58} of talus slope accumulations or rock glacier deposits⁵⁷, and from cosmogenic nuclide exposure age dating^{31,55,56}. Mid- to long-term rates potentially capture paraglacial and periglacial processes from pre-historical glacier recession and associated climate conditions (e.g. LIA or Younger Dryas; Fig. 1d). We compiled the mean, and the lower and upper range of the erosion rates to reflect the variability of erosion within catchments, and evaluated the relationship between erosion rate and elevation (Fig. 1b). If rockwall elevations were not reported in the original studies, they were derived from topographic maps or Google Earth.

Reconstruction of glacier retreat history of the Hungerli Valley. We used an orthophoto from 2017, historical photos, moraine locations and a regional study on LGM glacier thickness⁹⁵ to reconstruct the deglaciation history of the Hungerli Valley. To assess the locations and elevations of newly exposed rockwall as a result of glacier retreat since the LGM⁹⁶, we used a regional study that suggests an ice surface elevation of 2800 m⁹⁵ for the main trunk glacier in proximity to Hungerli Valley at the LGM. Based on the ice surface isoline, the glaciated areas at the LGM were coherently enlarged to the cirque and firm basin headwalls⁹⁷. For pre-historical rockwall exposure, we reconstructed the Egesen glaciation from mapped moraines (Supplementary Fig. 3e), previously correlated to Egesen age (11 ± 1 ka⁹⁶, equivalent to Younger Dryas)^{63,98}. We projected the moraine height to the rockwall (Fig. 2a) to approximate the ice surface at the rockwalls.

These approximate ice surface reconstructions suggest that the Rothorn cirque was fully glaciated during LGM and Egesen, while the upper Hungerlihorn peak (> 2800 m) remained ice-free. While our reconstruction approach provides only a crude approximation, we consider it acceptable for the purpose intended, and we account for uncertainty by applying a ± 50 m vertical buffer to our Egesen and LGM glacier extents, which is propagated into the calculated erosion rates. Reconstructions based on trimlines ignore small, cold-based glaciers that might have been present on higher parts of the rockwalls, and to examine the impact of this we included a scenario with a cold-based glacier on the Rothorn during the LGM.

Historical photos were used to reconstruct the exposure of new rockwall from the 19th century onwards. Historic photos were available for 1964⁹⁹, 1929 and 1882 (Supplementary Fig. 3a–c), and swissTopo provided a georeferenced orthophoto from summer 2017 (Fig. 2b). We reconstructed the glaciated area of the Rothorn cirque by using distinct landforms, ridges and mountain peaks, with an estimated vertical error of $\pm 5\%$.

Rock temperature measurements. To model frost cracking and mean annual rock surface temperature (MARST), we measured rock surface temperature (RST) at five rockwalls along a topographic gradient from 2580 to 3148 m (Fig. 2) using Maxim iButton DS1922L temperature loggers installed in 0.1 m deep boreholes, similar to previous studies^{32,78,91,100}. The loggers recorded RST at 3 h intervals (Supplementary Fig. 4) between 1 September 2016 and 31 August 2019 at RW2 and RW5, and between 29 August 2017 and 28 August 2019 at RW1. MARST was calculated to compare temperature logger locations and for permafrost modelling (Supplementary Table 2). The rockwall thermal regime is affected by snow cover, with a significant influence on permafrost distribution^{78,100–102} and frost

cracking^{32,103}. We examined the daily standard deviation in RST as a measure of snow cover, and applied a uniform threshold of < 0.5 °C for positive and negative RST following established practice^{78,100} (Supplementary Note 1).

Rock temperature modelling. We propagated measured rock surface temperature into the rockwalls by conductive heat transfer with latent heat effects at the phase transition between water and ice^{32,103}. Rock temperatures T over depth z and time t in one dimension were calculated by conservation of heat and Fourier's Law¹⁰⁴:

$$\frac{\partial T}{\partial t} = -\frac{1}{\rho_r c} \frac{\partial Q_h}{\partial z}, \quad Q_h = -\kappa \frac{\partial T}{\partial z} \quad (1)$$

where Q_h is vertical heat flux, ρ_r is rock density, c is specific heat capacity, and κ is thermal conductivity. Following the approach of previous studies^{32,103,105}, we used a temperature-dependent volumetric specific heat capacity C and thermal conductivity κ to consider latent heat L effects for the phase changing envelope DT , which was set between -1 and 0 °C:

$$\kappa = \begin{cases} \kappa_f, & T < T_f - DT \\ \lambda \kappa_f + \frac{\kappa_u - \kappa_f}{DT} [T - (T_f - DT)], & T_f - DT < T < T_f \\ \kappa_u, & T > T_f \end{cases} \quad (2)$$

$$C = \begin{cases} C_f, & T < T_f - DT \\ C_f + L \rho_b \frac{W - W_u}{DT}, & T_f - DT < T < T_f \\ C_u, & T > T_f \end{cases} \quad (3)$$

where the subscripts f and u stand for frozen and unfrozen, ρ_b is bulk (rock, water, ice) density, W reflects the total water content of the substrate as a fraction of mass, and W_u is the remaining unfrozen water content below $T_f = -1$ °C. W equals the porosity for unfrozen rock. We set W to 3% following previous rock temperature models^{32,78,89,106} and assumed a fully saturated rockwall, consistent with previous investigations of rock moisture measurements^{107,108}. For unfrozen water content W_u , we set a value 5%^{32,103}. Thermal conductivity κ and specific heat capacity c were geometrically weighted in the frozen and unfrozen region of the rock mass:

$$\kappa = \kappa_i^{\nu_i} \kappa_w^{\nu_w} \kappa_r^{\nu_r}, \quad c = c_i \nu_i + c_w \nu_w + c_r \nu_r \quad (4)$$

where i, w, r are the subscripts for ice, water, rock, and ν is the fractional content. The geology of the Hungerli Valley is predominantly paragneiss from the Mischabel nappe, consisting of schisty quartz slate with thin bands of aplite at the Rothorn cirque and intersections of amphibolite and aplite at the Hungerlihorn¹⁰⁹ (Supplementary Figs. 1 and 2). For the calculations, we used previously measured rock density data (Supplementary Table 3) and took published thermal conductivity λ and heat capacity c^{110} values for these rock types. To determine the temperature depth profile in each rockwall, we used our logged temperatures as rock surface temperatures, and applied Eqs. 1–4 with a spatial resolution Δz of 0.1 m. To evaluate the start conditions, we used a spin-up of 4 years on each temperature logger until steady-state rock temperature conditions were achieved^{32,78,105}. Rock temperature modelling revealed permafrost occurrence with 2 to 3 m active layer thawing at RW1–3, while seasonal freezing penetrated 2 to 4 m at RW4–5 (Supplementary Fig. 5).

Frost cracking modelling. To model frost cracking, we used our modelled rock temperature profiles to drive a frost cracking model (Supplementary Note 2). We applied a model that incorporates rock strength (Supplementary Table 3) and which assumes a porosity change to occur alongside frost cracking⁷². The model determines an upper temperature limit ΔT_c for segregation ice growth depending on rock strength:

$$\Delta T_c \approx \frac{T_m P_c}{\rho_i L} \text{ with } P_c = \frac{\sqrt{\pi} K_C}{2 \sqrt{x_i}} \quad (5)$$

where T_m is the bulk melting temperature, ρ_i ice density, L latent heat, P_c the critical ice pressure, K_C the critical fracture toughness, and x_i the crack radius. We incorporated rock strength by using critical fracture toughness previously determined for each lithology⁷³. The lower limit of ice segregation is controlled by water availability, which is determined by permeability:

$$k_{pf} = k_{p0} \left(\frac{\Delta T_f}{\Delta T} \right)^\alpha \quad (6)$$

where k_{pf} is the frozen and k_{p0} the unfrozen permeability, ΔT_f is the pore freezing point, α is a power law exponent, and ΔT is the temperature below the bulk freezing point. Water migration in the frozen fringe was calculated based on the unfrozen permeability of the rock mass, with a value of 10^{-18} m² adopted for all rockwalls (based on the permeability of schisty quartz slate¹¹¹). While permeability is likely heterogeneous within a single rockwall, and will vary slightly between the amphibolite and aplite lithologies, we consider it reasonable to assume a uniform value, consistent with existing model approaches^{72,83}. Sensitivity tests on permeability, initial crack length and fracture toughness demonstrated that while these factors affect the magnitude of frost cracking, they do not change the pattern of affected rock mass depth³².

To analyse the dependence of frost cracking on elevation, we calculated the total amount of permanent rock expansion (λ) induced by frost cracking at each rockfall⁷². Total rock expansion is a sum of the frost cracking intensity at different depths within the rockwall and is calculated here as:

$$\lambda = \frac{D}{\Delta T_c} \int_{1 \text{ year}} \left[\left(\frac{\Delta T_c}{\Delta T} \right)^\alpha \Big|_{z^+, \Delta T \geq \Delta T_c} - \left(\frac{\Delta T_c}{\Delta T} \right)^\alpha \frac{\partial T}{\partial z} \Big|_{z^-, \Delta T \geq \Delta T_c} \right] dt \quad (7)$$

The diffusivity D is

$$D = \frac{\alpha \rho L k_c \Delta T_c}{T_m \mu} \quad (8)$$

where α is a power law exponent and μ is the water viscosity⁷². Diffusivity is used as a measure of the propensity for frost-induced porosity changes. We calculated the total expansion separately for each year and lithology, to calculate a minimum, mean and maximum annual rock expansion total over the monitoring period (Supplementary Fig. 7). We consider the total rock expansion to represent the amount of (depth-integrated) frost cracking taking place at each rockfall.

Rockwall permafrost model. We used a multiple linear regression model fitted with multi-annual rock surface temperature (RST) measurements⁶⁷ to model rock permafrost distribution in the Hungerli Valley, taking into account the effects of snow cover limiting incoming solar radiation³². We simulated the potential incoming solar radiation (PISR) for each 2 m digital elevation model (DEM) raster cell using the area solar calculator of ESRI ArcGIS 10.7.1 for a snow-free period^{74,112,113} from June to October in hourly steps assuming an atmosphere with no diffusivity^{67,105,114,115}. The 'long-term' average length of the snow-free period was derived from a 20-year meteo station dataset¹¹⁶, located at Oberer Stelli Glacier in the Matter Valley. The station is 2–3 km SE of our study site at 2910 m elevation, and the snow duration at the meteo station corresponded well to snow cover in the Hungerli Valley for the 3-year period observed by our rock surface temperature measurements (Supplementary Fig. 8). To develop a statistical relationship between mean annual rock surface temperature (MARST) and the mean annual air temperature (MAAT) and PISR, we used temperature loggers at north and south facing slope aspects in the Hungerli Valley (two south facing loggers, RW1-S and RW2-S, and five north-facing loggers, RW1-5; Supplementary Table 4). We calculated MARST for each raster cell as:

$$\text{MARST}_{\text{pred}} = a + \text{PISR} * b + \text{MAAT} * c \quad (9)$$

with a , b and c representing calculated coefficients. For every logger location, we calculated the MAAT for the respective elevation using a temperature lapse rate of 6°C km^{-1} derived from a comparison of daily air temperature between meteo station Oberer Stelligletscher at 2910 m and a near-by meteo station, Grächen at 1605 m¹¹⁷. We tested the quality of the relationship using r^2 , mean absolute error (MSE) and root mean square error (RMS) (Supplementary Table 5). Similar to previous approaches, we applied a 30-year MAAT for the period 1990 to 2019 (Supplementary Table 4) to Eq. (9) for the rockwall area to incorporate the slow response time of rock permafrost^{67,114}. We interpret a $\text{MARST} \leq 0^\circ\text{C}$ as permafrost⁷⁴.

Laserscanning and rockfall detection. We scanned the rock faces in our study area from the opposing side of the valley floor, with a total of six positions (Fig. 2a), providing comprehensive coverage of all rockwalls. Due to the steep nature of the rockwalls, the oblique look-angle of our terrestrial laser scanning resulted in negligible scan shadowing (overcoming a limitation of aerial LiDAR scanning of steep rockwalls¹¹⁸). Only minor, gently sloping ledges, of little importance for rockfall generation¹¹⁹, were missed (confirmed by aerial LiDAR inspection). Laserscanning took place over four consecutive summers from 2016 to 2019 using Riegl VZ400 or Riegl VZ2000i scanners with identical accuracy (Supplementary Table 6). To produce a reference point cloud, we registered the 2017 scan positions by manually selecting several pairs of pseudo-homologous points. The point clouds were then aligned using an iterative-closest-point (ICP) algorithm^{120,121} implemented as the Multi Station Adjustment (MSA) in RiScan Pro 2.9. The basic assumption for this registration approach is that topographic change (i.e. rockfall) between scan epochs is negligibly small compared to the total scanned surface area used for point cloud alignment. To minimise registration errors, we excluded any non-rockwall surfaces (e.g. debris slopes). We applied the MSA algorithm to every subsequent scan from 2016, and 2018 to 2019 and registered each point cloud to our reference scan from 2017. The registration error lies between 2.7 and 5.0 cm, similar to that reported by others^{43,46,47,122,123}. An octree filter implemented in RiScan Pro was used to adapt all point clouds to a spatially continuous resolution of 0.1 m. We assumed that a rockfall event produces a distance difference between two point clouds, which we identified using the Multiscale Model to Model Cloud Comparison (M3C2) algorithm¹²⁴ implemented in Cloud Compare 2.9.1, similar to previous studies^{47,125,126}. The algorithm parameterizes surface roughness and alignment uncertainty to estimate a confidence interval, with a rockfall or movement recognised when the confidence interval is exceeded^{127,128}. In our analyses, we used the significant change option for determining rockfall with a projection scale of 1 m and a maximum depth of 15 m. Every identified potential rockfall event was analysed manually and visually, with its volume estimated using the cut-fill volume tool in RiScan Pro. Due to the annual resolution of our data collection

(i.e. long time between scans), it is likely that many 'events' assumed to be single rockfalls could have been multiple smaller rockfalls¹²⁹, which would affect our magnitude-frequency analyses. However, this issue has little bearing on the overall spatial patterns of our annual rockwall erosion rates, for which an annual scanning frequency is deemed suitable¹²⁶.

Statistical analysis of influencing factors. Environmental variables are often auto-correlated and a principal component analysis (PCA) can be used to find an axis or dimension that summarizes this redundancy¹³⁰. We applied a PCA using R software packages FactoMineR and ggplot to evaluate the relationships between rockfall variables similar to previous approaches^{131,132}. For each rockfall event, we extracted (i) elevation as a proxy for frost cracking, (ii) MARST as a proxy for permafrost, (iii) deglaciation age as a proxy for paraglacial adjustment, (iv) slope angle as a proxy for shear stress, and (v) rockfall volume. In using deglaciation age as a proxy for paraglacial process intensity we assumed that paraglacial processes were most intense at the start of deglaciation and decreased thereafter in the form of an exhaustion curve^{9,84}. We used the rockfall elevation as a proxy for frost cracking, which at the Hungerli Valley has been shown to strongly scale with elevation³² despite variability in lithology and other local influences^{73,87}. For each rockfall event, we extracted slope angle and rockfall volume from our laserscanning-derived DEM. All parameters were standardised using

$$\frac{x_i - \bar{x}}{\sigma} \quad (10)$$

where \bar{x} is the mean and σ is the standard deviation¹³⁰. To standardise slope angle, we converted degree angles to radians. We kept principal components with values >1 (PC1) or close to 1 (PC2; Supplementary Table 7 and Fig. 3b).

Derivation of short-term rockwall erosion rates. For evaluating the influence of elevation on rockwall erosion rates, we derived rockwall area within 100 m elevation bands (Supplementary Table 8). Based on our reconstructed glacier distribution, we calculated rockwall erosion rates for every deglaciation step (i.e. successively exposed rock wall area) incorporating a glacier extent uncertainty of $\pm 5\%$ for 2017, 1964, 1929 and 1882 glacier extents and an uncertainty of ± 50 m for Egesen and LGM glacier extents (Supplementary Table 9). We classified MARST into $<-3^\circ\text{C}$, -3 to -2°C , -2 to -1°C , -1 to 0°C and $>0^\circ\text{C}$ classes, similar to previous permafrost model approaches⁷⁴, and calculated the area and rockwall erosion rate for every MARST class (Supplementary Table 10). Area was calculated in Cloud Compare using the Poisson Surface Reconstruction tool^{133,134} to produce a mesh (with a relatively high octree depth of 10 to 12). The mesh was adjusted using the output density to optimise it for the input cloud, to capture the full complexity of the surface area, without over-smoothing data gaps and patchy areas of the point cloud.

Mid- and long-term rockwall erosion calculation using talus slopes. We selected only talus slopes that have not been reworked by rock glaciers for our analysis in the Hungerli Valley. We applied electric resistivity tomography (ERT) and seismic refraction tomography (SRT) in longitudinal transects from the rockwall to the toe of three talus slopes (Supplementary Note 3) to quantify the sediment thickness. For topographic corrections, we extracted elevations along each transect from the swissTopo Alti3D digital elevation model. ERT data were acquired using a Wenner-Schlumberger approach and were processed using Res2DInv with a resolution of half of the electrode spacing (Supplementary Table 11). The root mean square error (RMS) was used to provide an estimation of model quality, and the values were within the ranges found in previous talus slope studies^{51,135–138}. Seismic refraction signals were triggered by sledgehammer shots, recorded using a Geometrics Geode with 24 Geophones, and processed using ReflexW 9.1.3 (Supplementary Table 11). First-arrivals were picked manually^{139,140} to derive the travel-time of the refracted seismic waves, which were analysed to identify seismic layers^{139–141}. Layer properties were used to adjust initial starting models and gradients. Sediment thickness was interpreted from one-dimensional profiles of electrical resistivity and seismic velocity every 12.5 m (Supplementary Fig. 9). Talus slopes 2 and 3 indicated the possible presence of a basal moraine, which would result in smaller talus volumes. We accounted for this uncertainty by using two different basal talus surfaces in the volume calculations (with and without moraine). Talus slope volume (V_t) was calculated by subtracting the lower subsurface boundary from the talus ground surface using Golden Software Surfer 17. The rockwall erosion rate E_r was calculated as:

$$E_r = V_t \frac{\rho_t}{\rho_r A_r t} \quad (11)$$

where ρ_r is the density of the rockwall (2800 kg m^{-3} , Supplementary Table 3), ρ_t is talus density, A_r is the rockwall surface area providing rockfall material, and t is the time period of talus accumulation. Talus density varies vertically from 2000 kg m^{-3} near the surface to 2500 kg m^{-3} at the base¹⁴². We incorporated the entire range of talus density into our erosion rate calculation to avoid bias from densification⁶¹ if using only a single value. Talus age was derived from glacier reconstruction and ranged from 55 a (Talus slope-1) to 11 ± 1 ka (Talus slope-2 and -3). Rockwall surface area and talus slope surface area were both determined from the DEM with an assumed mapping uncertainty of $\pm 5\%$, which we included, along with potential moraine presence, in our erosion rate calculation (Supplementary Table 12). Mid-

to long-term erosion rates integrate changes in seismic activity⁸⁶ or climatic phases⁶⁰ and the influence should be similar in a single mountain range as the European Alps.

Data availability

The data that support the findings of this study are available at figshare (<https://doi.org/10.6084/m9.figshare.17152481.v1>)¹⁴³. For the regional analysis, we used freely available data including a 25 m digital elevation model of the European Alps provided by Copernicus (<https://land.copernicus.eu/imagery-in-situ/eu-dem/eu-dem-v1.1>), LGM extent (https://booksite.elsevier.com/9780444534477/DCW_Europe_WGS84.php) and permafrost extent (https://www.geo.uzh.ch/microsite/cryodata/PF_map_explanation.html). Digital elevation data (swissALTI3D; <https://www.swisstopo.admin.ch/de/geodata/height/alti3d.html>) and orthophoto (swissIMAGE25; <https://www.swisstopo.admin.ch/de/geodata/images/ortho/swissimage25.html>) is available from swissTopo. Meteo data used in this study is free available from MeteoSwiss (<https://gate.meteoswiss.ch/idaweb>).

Code availability

The authors declare that the code used to obtain the main results of this study can be made available from the corresponding author upon request.

Received: 29 September 2021; Accepted: 21 December 2021;

Published online: 09 February 2022

References

- Whipple, K. X. The influence of climate on the tectonic evolution of mountain belts. *Nat. Geosci.* **2**, 97–104 (2009).
- Whipple, K. X., Kirby, E. & Brocklehurst, S. H. Geomorphic limits to climate-induced increases in topographic relief. *Nature* **401**, 39–43 (1999).
- Egholm, D. L., Nielsen, S. B., Pedersen, V. K. & Lesemann, J. E. Glacial effects limiting mountain height. *Nature* **460**, 884–887 (2009).
- Brozovic, N., Burbank, D. W. & Meigs, A. J. Climatic limits on landscape development in the northwestern Himalaya. *Science* **276**, 571–574 (1997).
- Harbor, J. M., Hallet, B. & Raymond, C. F. A numerical model of landform development by glacial erosion. *Nature* **333**, 347 (1988).
- Hallet, B., Hunter, L. & Bogen, J. Rates of erosion and sediment evacuation by glaciers: a review of field data and their implications. *Glob. Planet. Change* **12**, 213–235 (1996).
- Pedersen, V. K., Egholm, D. L. & Nielsen, S. B. Alpine glacial topography and the rate of rock column uplift: a global perspective. *Geomorphology* **122**, 129–139 (2010).
- Mitchell, S. G. & Montgomery, D. R. Influence of a glacial buzzsaw on the height and morphology of the Cascade Range in central Washington State, USA. *Quat. Res.* **65**, 96–107 (2006).
- Ballantyne, C. K. Paraglacial geomorphology. *Quat. Sci. Rev.* **21**, 1935–2017 (2002).
- McCull, S. T. Paraglacial rock-slope stability. *Geomorphology* **153–154**, 1–16 (2012).
- McCull, S. T. & Draebing, D. in *Geomorphology of proglacial systems—Landform and sediment dynamics in recently deglaciated alpine landscapes* (eds Tobias Heckmann & D. Morche) 119–141 (Springer, 2019).
- Grämiger, L. M., Moore, J. R., Gischig, V. S., Ivy-Ochs, S. & Loew, S. Beyond debuitressing: mechanics of paraglacial rock slope damage during repeat glacial cycles. *J. Geophys. Res. Earth* **122**, 1004–1036 (2017).
- Grämiger, L. M., Moore, J. R., Gischig, V. S. & Loew, S. Thermo-mechanical stresses drive damage of Alpine valley rock walls during repeat glacial cycles. *J. Geophys. Res. Earth* **123**, 2620–2646 (2018).
- Grämiger, L. M. et al. Hydromechanical rock slope damage during Late Pleistocene and Holocene glacial cycles in an Alpine valley. *J. Geophys. Res. Earth* **125**, e2019JF005494 (2020).
- Leith, K., Moore, J. R., Amann, F. & Loew, S. Subglacial extensional fracture development and implications for Alpine Valley evolution. *J. Geophys. Res. Earth* **119**, 62–81 (2014).
- Leith, K., Moore, J. R., Amann, F. & Loew, S. In situ stress control on microcrack generation and macroscopic extensional fracture in exhuming bedrock. *J. Geophys. Res. Sol. Earth* **119**, 594–615 (2014).
- Köpfl, P., Grämiger, L. M., Moore, J. R., Vockenhuber, C. & Ivy-Ochs, S. The Oeschinensee rock avalanche, Bernese Alps, Switzerland: a co-seismic failure 2300 years ago? *Swiss J. Geosci.* **111**, 205–219 (2018).
- Oswald, P., Strasser, M., Hammerl, C. & Moernaut, J. Seismic control of large prehistoric rockslides in the Eastern Alps. *Nat. Commun.* **12**, 1059 (2021).
- Eppes, M.-C. & Keanini, R. Mechanical weathering and rock erosion by climate-dependent subcritical cracking. *Rev. Geophys.* **55**, 470–508 (2017).
- Matsuoka, N. & Murton, J. Frost weathering: Recent advances and future directions. *Permafrost Periglac.* **19**, 195–210 (2008).
- Krautblatter, M., Funk, D. & Günzel, F. K. Why permafrost rocks become unstable: a rock–ice-mechanical model in time and space. *Earth Surf. Proc. Land.* **38**, 876–887 (2013).
- Murton, J. B., Peterson, R. & Ozouf, J. C. Bedrock fracture by ice segregation in cold regions. *Science* **314**, 1127–1129 (2006).
- Draebing, D., Krautblatter, M. & Hoffmann, T. Thermo-cryogenic controls of fracture kinematics in permafrost rockwalls. *Geophys. Res. Lett.* **44**, 3535–3544 (2017).
- Krautblatter, M. & Dikau, R. Towards a uniform concept for the comparison and extrapolation of rockwall retreat and rockfall supply. *Geogr. Ann.* **A 89**, 21–40 (2007).
- Hales, T. C. & Roering, J. J. A frost “buzzsaw” mechanism for erosion of the eastern Southern Alps, New Zealand. *Geomorphology* **107**, 241–253 (2009).
- Vargo, L. J. et al. Anthropogenic warming forces extreme annual glacier mass loss. *Nat. Clim. Change* **10**, 856–861 (2020).
- Sommer, C. et al. Rapid glacier retreat and downwasting throughout the European Alps in the early 21st century. *Nat. Commun.* **11**, 3209 (2020).
- Farinotti, D. et al. A consensus estimate for the ice thickness distribution of all glaciers on Earth. *Nat. Geosci.* **12**, 168–173 (2019).
- Roe, G. H., Baker, M. B. & Herla, F. Centennial glacier retreat as categorical evidence of regional climate change. *Nat. Geosci.* **10**, 95–99 (2017).
- Girard, L., Gruber, S., Weber, S. & Beutel, J. Environmental controls of frost cracking revealed through in situ acoustic emission measurements in steep bedrock. *Geophys. Res. Lett.* **40**, 1748–1753 (2013).
- Mair, D. et al. The role of frost cracking in local denudation of steep Alpine rockwalls over millennia (Eiger, Switzerland). *Earth Surf. Dynam.* **8**, 637–659 (2020).
- Draebing, D. & Mayer, T. Topographic and geologic controls on frost cracking in Alpine rockwalls. *J. Geophys. Res. Earth* **126**, e2021JF006163 (2021).
- Biskaborn, B. K. et al. Permafrost is warming at a global scale. *Nat. Commun.* **10**, 264 (2019).
- Scandroglio, R., Draebing, D., Offer, M. & Krautblatter, M. 4D-Quantification of alpine permafrost degradation in steep rock walls using a laboratory-calibrated ERT approach. *Near Surf. Geophys.* **19**, 241–260 (2021).
- Harris, C. et al. Permafrost and climate in Europe: Monitoring and modelling thermal, geomorphological and geotechnical responses. *Earth-Sci. Rev.* **92**, 117–171 (2009).
- RGI Consortium. Randolph Glacier Inventory – A Dataset of Global Glacier Outlines: Version 6.0: Technical Report, Global Land Ice Measurements from Space, Colorado, USA. Digital Media (2017).
- Huss, M. & Fischer, M. Sensitivity of very small glaciers in the Swiss Alps to future climate change. *Front. Earth Sci.* **4**, 34 (2016).
- Boeckli, L., Brenning, A., Gruber, S. & Noetzi, J. Permafrost distribution in the European Alps: calculation and evaluation of an index map and summary statistics. *Cryosphere* **6**, 807–820 (2012).
- Haeblerli, W. In *Cryospheric Systems: Glaciers and Permafrost Vol. 242 Special Publications* (eds C. Harris & J. B. Murton) 29–37 (Geological Society, 2005).
- Mohadjer, S. et al. Temporal variations in rockfall and rock-wall retreat rates in a deglaciated valley over the past 11 k.y. *Geology* **48**, 594–598 (2020).
- Sass, O. Spatial patterns of rockfall intensity in the northern Alps. *Z. Geomorphol. Suppl.* **138**, 51–65 (2005).
- Kenner, R. Mass wasting processes affecting the surface of an alpine talus slope: annual sediment budgets 2009–2018 at Flüelapass, eastern Swiss Alps. *Land Degrad. Dev.* **31**, 451–462 (2020).
- Guerin, A., Ravanel, L., Matasci, B., Jaboyedoff, M. & Deline, P. The three-stage rock failure dynamics of the Drus (Mont Blanc massif, France) since the June 2005 large event. *Sci. Rep.* **10**, 17330 (2020).
- Hartmeyer, I. et al. Current glacier recession causes significant rockfall increase: the immediate paraglacial response of deglaciating cirque walls. *Earth Surf. Dynam.* **8**, 729–751 (2020).
- Kenner, R. et al. Investigation of rock and ice loss in a recently deglaciated mountain rock wall using terrestrial laser scanning: Gemsstock, Swiss Alps. *Cold Reg. Sci. Technol.* **67**, 157–164 (2011).
- Rabatel, A., Deline, P., Jaillat, S. & Ravanel, L. Rock falls in high-alpine rock walls quantified by terrestrial lidar measurements: a case study in the Mont Blanc area. *Geophys. Res. Lett.* **35**, L10502 (2008).
- Hartmeyer, I. et al. A 6-year lidar survey reveals enhanced rockwall retreat and modified rockfall magnitudes/frequencies in deglaciating cirques. *Earth Surf. Dynam.* **8**, 753–768 (2020).
- Haeblerli, W. et al. Pollen analysis and 14C age of moss remains in a permafrost core recovered from the active rock glacier Murtèl-Corvatsch, Swiss Alps: geomorphological and glaciological implications. *J. Glaciol.* **45**, 1–8 (1999).
- Krautblatter, M., Moser, M., Schrott, L., Wolf, J. & Morche, D. Significance of rockfall magnitude and carbonate dissolution for rock slope erosion and

- geomorphic work on Alpine limestone cliffs (Reintal, German Alps). *Geomorphology* **167**, 21–34 (2012).
50. Sass, O. Spatial and temporal patterns of talus activity – a lichenometric approach in the stubai alps, Austria. *Geogr. Ann.* **A 92**, 375–391 (2010).
 51. Sass, O. Bedrock detection and talus thickness assessment in the European Alps using geophysical methods. *J. Appl. Geophys.* **62**, 254–269 (2007).
 52. Sass, O. & Wollny, K. Investigations regarding Alpine talus slopes using ground-penetrating radar (GPR) in the Bavarian Alps, Germany. *Earth Surf. Proc. Land.* **26**, 1071–1086 (2001).
 53. Goetz, J., Otto, J. C. & Schrott, L. Postglacial sediment storage and rockwall retreat in a semi-closed inner-Alpine sedimentary basin (Gradenmoos, Hohe Tauern, Austria). *Geogr. Fis. Din. Quat.* **36**, 63–80 (2013).
 54. Hoffmann, T. & Schrott, L. Modelling sediment thickness and rockwall retreat in an Alpine valley using 2D seismic refraction (Reintal, Bavarian Alps). *Z. Geomorphol. Suppl.* **127**, 153–173 (2002).
 55. Lehmann, B. et al. Postglacial erosion of bedrock surfaces and deglaciation timing: new insights from the Mont Blanc massif (western Alps). *Geology* **48**, 139–144 (2019).
 56. Mair, D. et al. Fast long-term denudation rate of steep alpine headwalls inferred from cosmogenic ³⁶Cl depth profiles. *Sci. Rep.-UK* **9**, 11023 (2019).
 57. Barsch, D. *Rockglaciers. Indicators for the present and former geocology in high mountain environments.* (Springer, 1996).
 58. Kaiser, B. Variations spatiales et temporelles dans les rythmes d'évolution des versants alpins (Variability in time and space concerning alpine slope evolution). *Bull. Assoc. Geogr. Fr.* **69**, 265–270 (1992).
 59. Matthews, J. A. et al. Small rock-slope failures conditioned by Holocene permafrost degradation: a new approach and conceptual model based on Schmidt-hammer exposure-age dating, Jotunheimen, southern Norway. *Boreas* **47**, 1144–1169 (2018).
 60. Affolter, S. et al. Central Europe temperature constrained by speleothem fluid inclusion water isotopes over the past 14,000 years. *Sci. Adv.* **5**, eaav3809 (2019).
 61. Sadler, P. M. Sediment accumulation rates and the completeness of stratigraphic sections. *J. Geol.* **89**, 569–584 (1981).
 62. Ganti, V. et al. Time scale bias in erosion rates of glaciated landscapes. *Sci. Adv.* **2**, e1600204 (2016).
 63. Otto, J. C., Schrott, L., Jaboyedoff, M. & Dikau, R. Quantifying sediment storage in a high alpine valley (Turtmanntal, Switzerland). *Earth Surf. Proc. Land.* **34**, 1726–1742 (2009).
 64. Linsbauer, A. et al. The New Swiss Glacier Inventory SGI2016: from a topographical to a glaciological dataset. *Front. Earth Sci.* **9**, 774 (2021).
 65. Nyenhuis, M., Hoelzle, M. & Dikau, R. Rock glacier mapping and permafrost distribution modelling in the Turtmanntal, Valais, Switzerland. *Z. Geomorphol.* **49**, 275–292 (2005).
 66. Ravel, L., Magnin, F. & Deline, P. Impacts of the 2003 and 2015 summer heatwaves on permafrost-affected rock-walls in the Mont Blanc massif. *Sci. Total Environ.* **609**, 132–143 (2017).
 67. Magnin, F. et al. Permafrost distribution in steep rock slopes in Norway: measurements, statistical modelling and implications for geomorphological processes. *Earth Surf. Dynam.* **7**, 1019–1040 (2019).
 68. Montgomery, D. R. & Brandon, M. T. Topographic controls on erosion rates in tectonically active mountain ranges. *Earth Planet. Sc. Lett.* **201**, 481–489 (2002).
 69. Schmidt, K. M. & Montgomery, D. R. Limits to relief. *Science* **270**, 617–620 (1995).
 70. MacGregor, K. R., Anderson, R. S. & Waddington, E. D. Numerical modeling of glacial erosion and headwall processes in alpine valleys. *Geomorphology* **103**, 189–204 (2009).
 71. Alley, R. B., Cuffey, K. M. & Zoet, L. K. Glacial erosion: status and outlook. *Ann. Glaciol.* **60**, 1–13 (2019).
 72. Rempel, A. W., Marshall, J. A. & Roering, J. J. Modeling relative frost weathering rates at geomorphic scales. *Earth Planet. Sc. Lett.* **453**, 87–95 (2016).
 73. Draebing, D. & Krautblatter, M. The efficacy of frost weathering processes in Alpine rockwalls. *Geophys. Res. Lett.* **46**, 6516–6524 (2019).
 74. Kenner, R., Noetzi, J., Hoelzle, M., Raetz, H. & Phillips, M. Distinguishing ice-rich and ice-poor permafrost to map ground temperatures and ground ice occurrence in the Swiss Alps. *Cryosphere* **13**, 1925–1941 (2019).
 75. Mamot, P., Weber, S., Lanz, M. & Krautblatter, M. Brief communication: The influence of mica-rich rocks on the shear strength of ice-filled discontinuities. *Cryosphere* **14**, 1849–1855 (2020).
 76. Mamot, P., Weber, S., Schröder, T. & Krautblatter, M. A temperature- and stress-controlled failure criterion for ice-filled permafrost rock joints. *Cryosphere* **12**, 3333–3353 (2018).
 77. Davies, M. C. R., Hamza, O. & Harris, C. The effect of rise in mean annual temperature on the stability of rock slopes containing ice-filled discontinuities. *Permafrost Periglac.* **12**, 137–144 (2001).
 78. Draebing, D., Haberkorn, A., Krautblatter, M., Kenner, R. & Phillips, M. Thermal and mechanical responses resulting from spatial and temporal snow cover variability in permafrost Rock Slopes, Steintaelli, Swiss Alps. *Permafrost Periglac.* **28**, 140–157 (2017).
 79. Scherler, D. Climatic limits to headwall retreat in the Khumbu Himalaya, eastern Nepal. *Geology* **42**, 1019–1022 (2014).
 80. Delunel, R., van der Beek, P. A., Carcaillet, J., Bourles, D. L. & Valla, P. G. Frost-cracking control on catchment denudation rates: Insights from in situ produced Be-10 concentrations in stream sediments (Ecrins-Pelvoux massif, French Western Alps). *Earth Planet. Sc. Lett.* **293**, 72–83 (2010).
 81. von Blanckenburg, F. The control mechanisms of erosion and weathering at basin scale from cosmogenic nuclides in river sediment. *Earth Planet. Sc. Lett.* **237**, 462–479 (2005).
 82. Nishiyama, R. et al. Bedrock sculpting under an active alpine glacier revealed from cosmic-ray muon radiography. *Sci. Rep.* **9**, 6970 (2019).
 83. Sanders, J. W., Cuffey, K. M., Moore, J. R., MacGregor, K. R. & Kavanaugh, J. L. Periglacial weathering and headwall erosion in cirque glacier bergschrunds. *Geology* **40**, 779–782 (2012).
 84. Church, M. & Ryder, J. M. Paraglacial sedimentation: a consideration of fluvial processes conditioned by glaciation. *Geol. Soc. Am. Bull.* **83**, 3059–3071 (1972).
 85. Draebing, D., Krautblatter, M. & Dikau, R. Interaction of thermal and mechanical processes in steep permafrost rock walls: A conceptual approach. *Geomorphology* **226**, 226–235 (2014).
 86. Schweizerischer Erdbebendienst: ECOS. Earthquake Catalogue of Switzerland (2019).
 87. Walder, J. & Hallet, B. A theoretical-model of the fracture of rock during freezing. *Geol. Soc. Am. Bull.* **96**, 336–346 (1985).
 88. Myhra, K. S., Westermann, S. & Etzelmüller, B. Modelled distribution and temporal evolution of permafrost in steep rock walls along a latitudinal transect in Norway by CryoGrid 2D. *Permafrost Periglac.* **28**, 172–182 (2017).
 89. Wegmann, M., Gudmundsson, G. H. & Haeblerli, W. Permafrost Changes in Rock Walls and the retreat of alpine glaciers: a Thermal Modelling Approach. *Permafrost Periglac.* **9**, 23–33 (1998).
 90. Deprez, M., De Kock, T., De Schutter, G. & Cnudde, V. A review on freeze-thaw action and weathering of rocks. *Earth-Sci. Rev.* **203**, 103143 (2020).
 91. Draebing, D. Identification of rock and fracture kinematics in high Alpine rockwalls under the influence of elevation. *Earth Surf. Dynam.* **9**, 977–994 (2021).
 92. Eppes, M. C. et al. Deciphering the role of solar-induced thermal stresses in rock weathering. *Geol. Soc. Am. Bull.* **128**, 1315–1338 (2016).
 93. Eppes, M. C. et al. Warmer, wetter climates accelerate mechanical weathering in field data, independent of stress-loading. *Geophys. Res. Lett.* **47**, 2020GL089062 (2020).
 94. Collins, B. D. & Stock, G. M. Rockfall triggering by cyclic thermal stressing of exfoliation fractures. *Nat. Geosci.* **9**, 395–400 (2016).
 95. Kelly, M. A., Buoncristiani, J. F. & Schlüchter, C. A reconstruction of the last glacial maximum (LGM) ice-surface geometry in the western Swiss Alps and contiguous Alpine regions in Italy and France. *Eclogae Geol. Helv.* **57**, 57–75 (2004).
 96. Ivy-Ochs, S. et al. Chronology of the last glacial cycle in the European Alps. *J. Quat. Sc.* **23**, 559–573 (2008).
 97. Wirsig, C. et al. A deglaciation model of the Oberhasli, Switzerland. *J. Quaternary Sci.* **31**, 46–59 (2016).
 98. Otto, J. C. & Sass, O. Comparing geophysical methods for talus slope investigations in the Turtmann valley (Swiss Alps). *Geomorphology* **76**, 257–272 (2006).
 99. Swissair Photo AG. Turtmanntal, Barrhorn (1964).
 100. Haberkorn, A. et al. Thermal regime of rock and its relation to snow cover in steep alpine rock walls: Gemsstock. *Central Swiss Alps. Geogr. Ann.* **A 97**, 579–597 (2015).
 101. Haberkorn, A., Hoelzle, M., Phillips, M. & Kenner, R. Snow as a driving factor of rock surface temperatures in steep rough rock walls. *Cold Reg. Sci. Technol.* **118**, 64–75 (2015).
 102. Phillips, M., Haberkorn, A. & Rhyner, H. Snowpack characteristics on steep frozen rock slopes. *Cold Reg. Sci. Technol.* **141**, 54–65 (2017).
 103. Anderson, R. S., Anderson, S. P. & Tucker, G. E. Rock damage and regolith transport by frost: an example of climate modulation of the geomorphology of the critical zone. *Earth Surf. Proc. Land.* **38**, 299–316 (2013).
 104. Carslaw, H. S. & Jaeger, J. C. *Conduction of heat in solids.* 2nd edn, (Clarendon Press, 1986).
 105. Hipp, T., Etzelmüller, B. & Westermann, S. Permafrost in Alpine Rock Faces from Jotunheimen and Hurrungane. *Southern Norway. Permafrost Periglac.* **25**, 1–13 (2014).
 106. Noetzi, J., Gruber, S., Kohl, T., Salzmann, N. & Haeblerli, W. Three-dimensional distribution and evolution of permafrost temperatures in idealized high-mountain topography. *J. Geophys. Res.-Earth* **112**, F02S13 (2007).

107. Rode, M., Schnepfleiter, H. & Sass, O. Simulation of moisture content in alpine rockwalls during freeze–thaw events. *Earth Surf. Proc. Land*, **41**, 1937–1950 (2016).
108. Sass, O. Rock moisture measurements: techniques, results, and implications for weathering. *Earth Surf. Proc. Land*, **30**, 359–374 (2005).
109. Bearth, P. Geologischer Atlas der Schweiz 1:25000. Erläuterungen zum Atlasblatt 71 (1308 St. Niklaus). (Schweizer Geologische Kommission, 1980).
110. Cermák, V. & Rybach, L. In *Landolt–Börnstein Zahlenwerte und Funktionen aus Naturwissenschaften und Technik, Neue Serie, Physikalische Eigenschaften der Gesteine (V/1a)* (ed. G. Angeneister) 305–343 (Springer, 1982).
111. Krautblatter, M. *Detection and quantification of permafrost change in alpine rock walls and implications for rock instability* PhD Thesis thesis, Universität Bonn, (2009).
112. Hoelzle, M. Mapping and modelling of mountain permafrost distribution in the Alps. *Norsk Geogr. Tidsskr.* **50**, 11–15 (1996).
113. Hoelzle, M. & Haeblerli, W. Simulating the effects of mean annual air-temperature changes on permafrost distribution and glacier size: an example from the Upper Engadin, Swiss Alps. *Ann. Glaciol.* **21**, 399–405 (1995).
114. Boeckli, L., Brenning, A., Gruber, S. & Noetzli, J. A statistical approach to modelling permafrost distribution in the European Alps or similar mountain ranges. *Cryosphere* **6**, 125–140 (2012).
115. Magnin, F., Brenning, A., Bodin, X., Deline, P. & Ravel, L. Statistical modelling of rock wall permafrost distribution: application to the Mont Blanc massif. *Geomorphologie* **21**, 145–162 (2015).
116. MeteoSwiss. Climate data station Oberer Stelligletscher 2000–2019. Provided by MeteoSwiss, the Swiss Federal Office of Meteorology and Climatology (2019).
117. MeteoSwiss. Climate data station Grächen, 2000–2019. Provided by MeteoSwiss, the Swiss Federal Office of Meteorology and Climatology (2019).
118. Abellan, A. et al. Terrestrial laser scanning of rock slope instabilities. *Earth Surf. Proc. Land* **39**, 80–97 (2014).
119. Matasci, B. et al. Assessing rockfall susceptibility in steep and overhanging slopes using three-dimensional analysis of failure mechanisms. *Landslides* **15**, 859–878 (2017).
120. Chen, Y. & Medioni, G. Object modelling by registration of multiple range images. *Image Vision Comput* **10**, 145–155 (1992).
121. Besl, P. & McKay, N. Method for registration of 3-D shapes. Vol. 1611 (Proceedings Volume 1611, Sensor Fusion IV: Control Paradigms and Data Structures, 1992).
122. Rosser, N., Lim, M., Petley, D., Dunning, S. & Allison, R. Patterns of precursory rockfall prior to slope failure. *J. Geophys. Res.-Earth* **112**, F04014 (2007).
123. Abellán, A., Vilaplana, J. M., Calvet, J., García-Sellés, D. & Asensio, E. Rockfall monitoring by Terrestrial Laser Scanning – case study of the basaltic rock face at Castellfollit de la Roca (Catalonia, Spain). *Nat. Hazard. Earth Syst* **11**, 829–841 (2011).
124. Lague, D., Brodu, N. & Leroux, J. Accurate 3D comparison of complex topography with terrestrial laser scanner: Application to the Rangitikei canyon (N-Z). *ISPRS J. Photogram* **82**, 10–26 (2013).
125. James, M. R., Robson, S. & Smith, M. W. 3-D uncertainty-based topographic change detection with structure-from-motion photogrammetry: precision maps for ground control and directly georeferenced surveys. *Earth Surf. Proc. Land*, **42**, 1769–1788 (2017).
126. Williams, J. G., Rosser, N. J., Hardy, R. J., Brain, M. J. & Afana, A. A. Optimising 4-D surface change detection: an approach for capturing rockfall magnitude–frequency. *Earth Surf. Dynam* **6**, 101–119 (2018).
127. Soudarissanane, S., Lindenbergh, R., Menenti, M. & Teunissen, P. Scanning geometry: Influencing factor on the quality of terrestrial laser scanning points. *ISPRS J. Photogram* **66**, 389–399 (2011).
128. Hodge, R. A. Using simulated Terrestrial Laser Scanning to analyse errors in high-resolution scan data of irregular surfaces. *ISPRS J. Photogram* **65**, 227–240 (2010).
129. Williams, J. G., Rosser, N. J., Hardy, R. J. & Brain, M. J. The importance of monitoring interval for rockfall magnitude-frequency estimation. *J. Geophys. Res.-Earth* **124**, 2841–2853 (2019).
130. Leyer, I. & Wesche, K. *Multivariate Statistik in der Ökologie*. (Springer, 2007).
131. Crippa, C. et al. Semi-automated regional classification of the style of activity of slow rock-slope deformations using PS InSAR and SqueeSAR velocity data. *Landslides* **18**, 2445–2463 (2021).
132. Messenzehl, K., Viles, H., Otto, J.-C., Ewald, A. & Dikau, R. Linking rock weathering, rockfall instability and rockfall supply on talus slopes in glaciated hanging valleys (Swiss Alps). *Permafrost Periglac* **29**, 135–151 (2018).
133. Kazhdan, M., Bolitho, M. & Hoppe, H. Poisson surface reconstruction. In *Proceedings of the fourth Eurographics symposium on Geometry processing*. (2006).
134. Kazhdan, M. & Hoppe, H. Screened poisson surface reconstruction. *ACM Trans. Graph.* **32**, Article 29 (2013).
135. Kneisel, C. The nature and dynamics of frozen ground in alpine and subarctic periglacial environments. *Holocene* **20**, 423–445 (2010).
136. Kneisel, C. Assessment of subsurface lithology in mountain environments using 2D resistivity imaging. *Geomorphology* **80**, 32–44 (2006).
137. Kenner, R. et al. New insights on permafrost genesis and conservation in talus slopes based on observations at Flüelapass, Eastern Switzerland. *Geomorphology* **290**, 101–113 (2017).
138. Brody, A. G., Pluhar, C. J., Stock, G. M. & Greenwood, W. J. Near-surface geophysical imaging of a talus deposit in Yosemite Valley, California. *Environ. Eng. Geosci.* **21**, 111–127 (2015).
139. Krautblatter, M. & Draebing, D. Pseudo 3D - P-wave refraction seismic monitoring of permafrost in steep unstable bedrock. *J. Geophys. Res. Earth* **119**, 287–299 (2014).
140. Cody, E., Draebing, D., McColl, S., Cook, S. & Brideau, M.-A. Geomorphology and geological controls of an active paraglacial rockslide in the New Zealand Southern Alps. *Landslides* **17**, 755–776 (2020).
141. Hilbich, C. Time-lapse refraction seismic tomography for the detection of ground ice degradation. *Cryosphere* **4**, 243–259 (2010).
142. Scapozza, C., Baron, L. & Lambiel, C. Borehole Logging in Alpine Periglacial Talus Slopes (Valais, Swiss Alps). *Permafrost Periglac* **26**, 67–83 (2015).
143. Draebing, D., Mayer, T., Jacobs, B. & McColl, S. T. Alpine rockwall erosion patterns follow elevation-dependent climate trajectories. Data set. Figshare (2021).
144. Ehlers, J., Gibbard, P. L. & Hughes, P. D. *Quaternary Glaciations - Extent and Chronology*. Vol. 15 (Elsevier, 2011).

Acknowledgements

This study was funded by the German Research Foundation (DR1070/1-1). S.M. acknowledges additional funding by the Technical University of Munich and its August-Wilhelm Scheer Visiting Professor programme. We thank all students involved in fieldwork for their support. The authors acknowledge the valuable comments by five anonymous reviewers that helped to improve the manuscript. D.D. thanks Michael Krautblatter and Maarten Kleinans for hospitality.

Author contributions

All authors contributed to field data collection. T.M. and B.J. processed the laserscanning data. T.M. and D.D. performed the frost cracking modelling. D.D. designed the research set up, the study, modelled the permafrost distribution, and analysed the data and D.D. and S.M. wrote the manuscript with input from all authors.

Funding

Open Access funding enabled and organized by Projekt DEAL.

Competing interests

The authors declare no competing interests.

Additional information

Supplementary information The online version contains supplementary material available at <https://doi.org/10.1038/s43247-022-00348-2>.

Correspondence and requests for materials should be addressed to Daniel Draebing.

Peer review information *Communications Earth & Environment* thanks Arjun Heimsath, Ludovic Ravel and the other, anonymous, reviewer(s) for their contribution to the peer review of this work. Primary Handling Editors: Clare Davis. Peer reviewer reports are available.

Reprints and permission information is available at <http://www.nature.com/reprints>

Publisher's note Springer Nature remains neutral with regard to jurisdictional claims in published maps and institutional affiliations.



Open Access This article is licensed under a Creative Commons Attribution 4.0 International License, which permits use, sharing, adaptation, distribution and reproduction in any medium or format, as long as you give appropriate credit to the original author(s) and the source, provide a link to the Creative Commons license, and indicate if changes were made. The images or other third party material in this article are included in the article's Creative Commons license, unless indicated otherwise in a credit line to the material. If material is not included in the article's Creative Commons license and your intended use is not permitted by statutory regulation or exceeds the permitted use, you will need to obtain permission directly from the copyright holder. To view a copy of this license, visit <http://creativecommons.org/licenses/by/4.0/>.

© The Author(s) 2022



Holocene warming of alpine rockwalls decreased rockwall erosion rates

Daniel Draebing^{a,b,*}, Till Mayer^{b,c}, Benjamin Jacobs^c, Steven A. Binnie^d,
Miriam Dühnforth^{e,f,1}, Samuel T. McColl^g

^a Department of Physical Geography, Utrecht University, Princetonlaan 8a, 3584 CB Utrecht, the Netherlands¹

^b Chair of Geomorphology, University of Bayreuth, Universitätsstr. 30, 95447 Bayreuth, Germany

^c Chair of Landslide Research, Technical University of Munich, Arcisstr. 21, 80333 Munich, Germany

^d Department of Geology and Mineralogy, University of Cologne, Zùlpicher Str. 49b, 50674 Cologne, Germany

^e Versicherungskammer Bayern, Maximilianstraße 53, 80530 Munich, Germany¹

^f Department of Geology, Ludwig Maximilian University Munich, Luisenstr. 37, 80333 Munich, Germany

^g GNS Science, 1 Fairway Drive, Avalon 5010, New Zealand

ARTICLE INFO

Keywords:

Erosion
Frost weathering
Permafrost
Glacier
Paraglacial processes
Rockfall

ABSTRACT

Alpine rockwall erosion studies suggest that deglaciated rockwalls in the European Alps are eroding slower today than at earlier times in the Holocene. Explanations for this have included a waned glacial debuttressing effect since the retreat of Last Glacial ice loads and the establishment of more moderate climates, but seldom have such explanations been robustly tested. We combine field data with modelling to reconstruct changes in rockwall erosion and associated climate drivers, in an alpine valley of the European Alps since the beginning of the Holocene. Paleo (Holocene to decadal-scale) erosion rates were calculated from talus accumulation below rockwalls, and compared with recent rates (2016–2019) measured from repeat laserscan surveys of the same rockwalls. We reconstructed the glacial retreat history in the valley, and modelled Holocene changes in permafrost distribution and frost cracking using calibrated rockwall temperature reconstructions. We found that rockwalls that have been free of glacier ice since ~10 ka experienced higher Holocene-averaged erosion rates compared to recent erosion rates. Our modelling suggests this relates to periods of higher intensities of frost cracking and cycles of permafrost aggradation and degradation in the Holocene, relative to today. For a recently deglaciated high-elevation rockwall, erosion rates were 1–2 orders of magnitude greater than the lower-elevation sites, but decayed rapidly over time since deglaciation. A high, but rapidly decaying rate results from short-lived paraglacial adjustment, permafrost thaw and high frost cracking activity. Our findings suggest that periglacial activity strongly influences the rates and patterns of erosion of deglaciated alpine rockwalls. This helps to explain why paleo Holocene deglaciated rockwall erosion rates tend to exceed recent rates in the European Alps.

1. Introduction

Rockfall is the dominant process of rockwall erosion, and erodes landscapes in the European Alps at rates that are in the range of glacial erosion rates (0.5–36 mm a⁻¹; Cook et al., 2020). Studies of recent (i.e. present day to decades) rockwall erosion rates have identified rates between 0.05^{+0.03}_{-0.03} and 1.9^{+8.4}_{-1.6} mm a⁻¹, with localised, short-term rates at deglaciating headwalls or rockwalls with degrading permafrost of between 6.5 and 14.4 mm a⁻¹ (see compilation by Draebing et al., 2022). Studies of rates averaged over the Holocene have shown, with the exception of localized cases, rates are an order-of-magnitude higher

(0.252^{+0.148}_{-0.142} - 3.2^{+1.3}_{-1.8} mm a⁻¹) than recent rates (see compilation by Draebing et al., 2022). These differences likely relate to changes in climate, which in turn influence glacial and periglacial processes and the distribution and intensity of permafrost (Draebing et al., 2022).

Glacial processes influence paraglacial rockfall, which is rockfall that is directly conditioned by glacial activity (McColl, 2012; McColl and Draebing, 2019). Rockfall can be prepared and triggered by changes in rockwall stability (Leith et al., 2014) and seismic activity (e.g. Ballantyne et al., 2014) induced by changing glacier ice loads. Large rockslope failures have a response time to these changes on the order of millennia (Grämiger et al., 2017; McColl, 2012), while smaller-scale rockfalls may

* Corresponding author.

E-mail address: d.draebing@uu.nl (D. Draebing).

¹ Present address.

respond much faster (e.g. Hartmeyer et al., 2020). Periglacial processes influence rockfall through the breakdown of rock by frost cracking (Draebing and Krautblatter, 2019). Frost cracking activity has been invoked to explain major patterns of multidecadal rockfall activity (Savi et al., 2021) and postglacial catchment-wide erosion (Delunel et al., 2010; Savi et al., 2015). Permafrost affects rockwall stability in two opposite ways. Permafrost warming and thawing decreases rockwall strength rapidly (Krautblatter et al., 2013) and prepares and triggers rockfall (McCull and Draebing, 2019). Increasing rockfall activity in permafrost areas has been observed following short-term warm phases (Raveland et al., 2017) or warming since the Little Ice Age (Raveland and Deline, 2010). In contrast, permafrost aggradation (areal extension) following glacier retreat (Wegmann et al., 1998) or seasonal refreezing in winter produces cryogenic stresses (Draebing et al., 2017b) able to trigger rockfalls (Phillips et al., 2016).

Numerous studies reconstructed catchment-wide erosion rates from fluvial sediments at the outlet (e.g. Delunel et al., 2020) or sediment sinks as lakes or reservoirs (e.g. Hinderer et al., 2013), however, by increasing the spatial scale more landforms occur that can temporally disconnect sediment transport (Fryirs et al., 2007) and remobilization of stored sediment can temporally increase sediment yields (Church and Slaymaker, 1989) both complicating the analysis of climatic drivers of erosion. In contrast, rockwalls present the top of the sediment cascade in alpine environments and analysing preserved sediment deposits as talus

slopes or rock slope failure deposits can enable the identification of drivers of rockwall erosion (Hales and Roering, 2009; Matthews et al., 2018). Unfortunately, the relative effect of these drivers on rockwall erosion and their contribution to differences between recent and paleo rates is unknown. Much existing rockwall erosion data have been sourced from multiple methods and catchments with differing geology, elevation, and glacial history. Moreover, few studies have investigated both recent and paleo (Holocene-averaged) rockwall erosion within the same alpine catchment. While these few studies have demonstrated that paleo rates exceed recent erosion rates (Mohadjer et al., 2020; Sass, 2005), they have not been able to quantitatively and systematically conclude to what extent these patterns result from the effects of paraglacial and periglacial processes, or permafrost changes. Until these contributions can be quantified, accurate prediction of rockwall erosion and rockfall hazard in alpine areas in response to forecast climate changes remains out of reach.

Robustly evaluating why paleo rates exceed recent rates can be achieved by using quantitative and systematic approaches that combine field-based data with models. We achieved this by investigating changes in Holocene rockwall erosion in a catchment where erosion could be closely related to the geology, climate, glacial history, and elevation. We reconstructed the Early Holocene to present-day glacier retreat, permafrost distribution, and frost-cracking patterns, and compared these to changes in rockfall activity recorded by laserscanning surveys

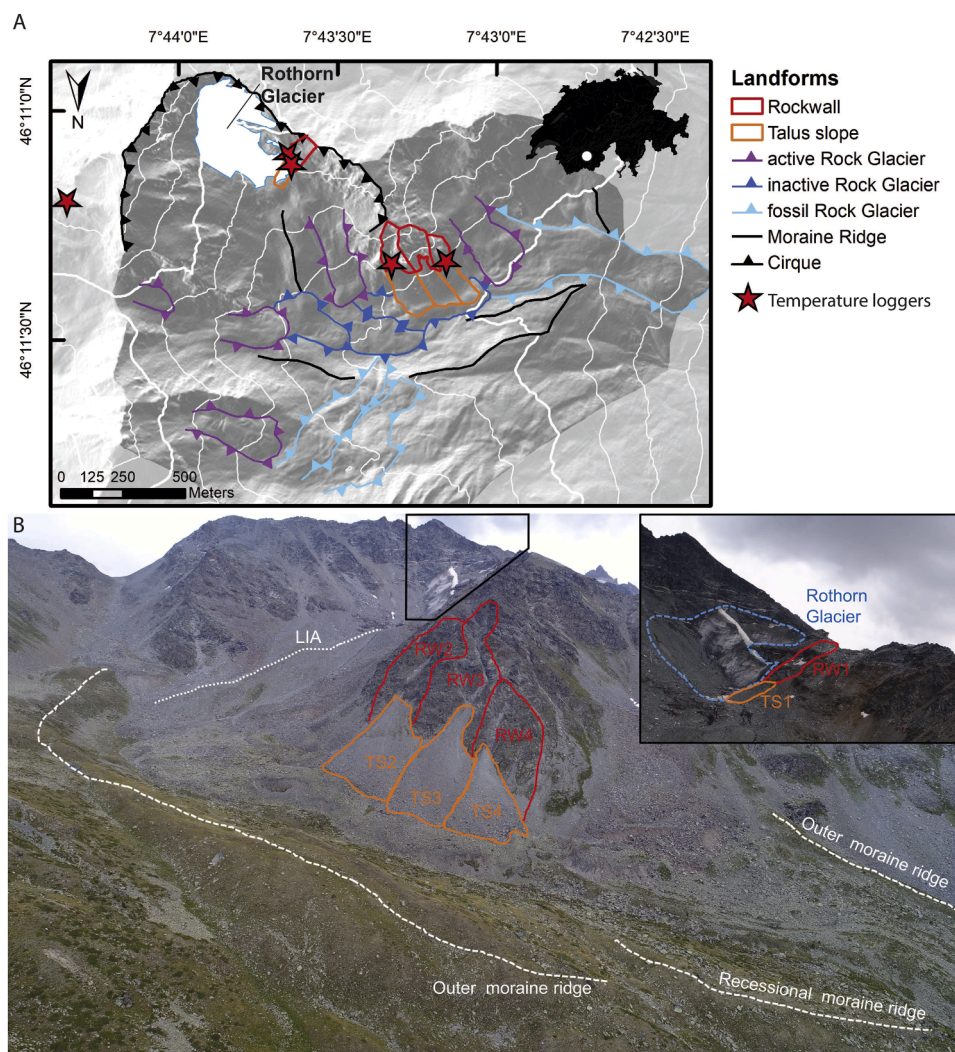


Fig. 1. (A) Hillshade of the Hungerli Valley with the modern glacier distribution and key landforms (source: swissALTI3d from swissTopo). Inset map show location within Switzerland. (B) Photo of investigated rockwalls, talus slopes and moraines.

and dated talus slope accumulations.

2. Study area

The Hungerli Valley (Fig. 1) is a hanging valley of the Turtmann Valley in the southern Swiss Alps. It has been a closed sediment system during the Holocene, disconnected from the main valley (Otto et al., 2009). The valley has steep rockwalls, from 2500 to 3277 m elevation of predominantly paragneiss, consisting of schisty quartz slate with aplite and amphibolite bands. Today, ice of the Rothorn Glacier is limited to

the small Rothorn Cirque, but an expanded Holocene extent is evidenced by Little Ice Age (LIA) and older moraines within the hanging valley (Fig. 1). Regional glacier models suggest that Last Glacial Maximum (LGM) trimlines were at elevations of up to 2700 m (Kelly et al., 2004), suggesting much of the rockwall area in the Hungerli Valley was glacier-free. Historic photos show the Rothorn Glacier in contact with rockwalls of only the Rothorn Cirque by the end of the LIA (Fig. S2). In this study we investigated four rockwalls and their associated talus slopes in the Hungerli Valley (Fig. 1). All four rockwalls are affected by permafrost and frost cracking (Draebing and Mayer, 2021; Draebing

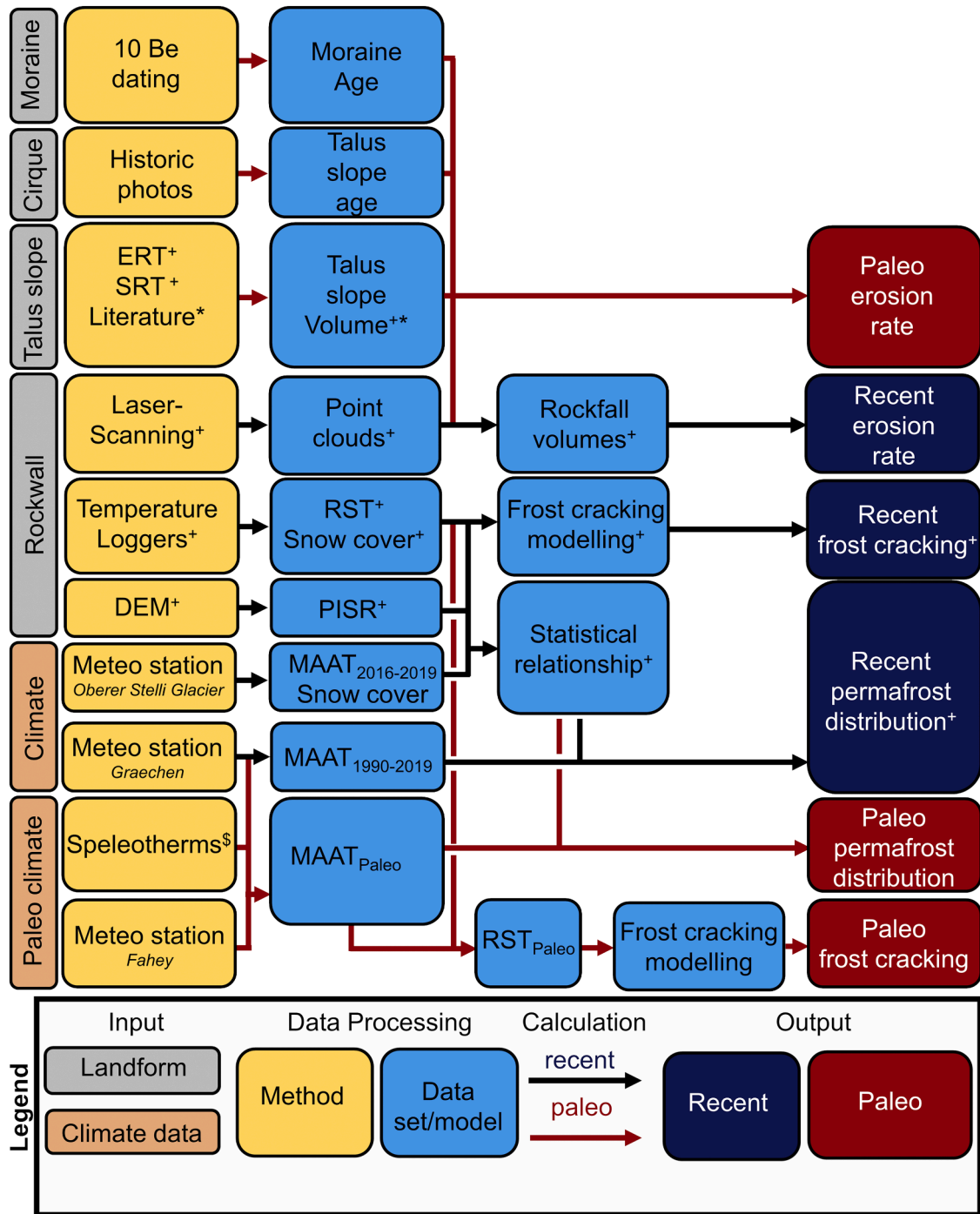


Fig. 2. Applied data sets and techniques to calculate paleo (Holocene to decadal timescale) and recent (2016–2019) frost cracking, permafrost distribution and erosion rates (data collected and processed by ⁺Draebing et al., 2022, ^{*}Otto and Sass, 2006 and [§]Affolter et al., 2019). ERT = Electrical Resistivity Tomography, SRT = Seismic Refraction Tomography, DEM = Digital Elevation Model, RST = Rock Surface Temperature, PISR = Potential Incoming Solar Radiation, MAAT = Mean Annual Air Temperature.

et al., 2022), and one is located near to the Rothorn Glacier terminus (Fig. 1).

3. Methods

Based on landforms and climate data, we applied different methods (Fig. 2) to reconstruct the glacial history (3.1), measure present air and rock temperatures (3.2), reconstruct past air and rock surface temperatures (3.3), model rock permafrost (3.4) and frost cracking (3.5), and quantify recent and paleo rockwall erosion rates (3.6). In this study, by ‘recent’ we refer to rockwall rates measured annually over a four year period (2016–2019). By ‘paleo’ we refer to rates that were averaged over the time period of talus slope accumulation in the order of 9–10 ka, but also include one site for which the erosion was averaged over the past five decades. For convenience we refer to this decadal average as ‘paleo’, to distinguish it from the ‘recent’ rates.

3.1. Reconstruction of glacier retreat history for measurement of paleo rockwall erosion

The paleo rockwall erosion rates were evaluated from accumulation of talus below several rockwalls in the valley (Fig. 1). To estimate the duration (integration time) of talus accumulation required for the paleo erosion rate calculations (Section 3.6), we dated moraines adjacent to the talus slopes. The moraines provide maximum constraining ages for the talus slopes because debris could not have accumulated while the moraines were forming (Fig. 1). To date the pre-historical moraines, rock samples were collected from the top of moraine boulders located on an outer moraine ridge (samples Mo1–6) and on a recessional moraine ridge (Mo7–9; Fig. 1) for Be-10 surface exposure dating. Sampled boulders were large ($>5\text{ m}^3$), in a stable position and the top of each boulder was at least 1.6 m above the surrounding ground surface to minimize the effect of snow cover (Fig. 3). Surface-exposure ages were computed with the CRONUS calculator (Balco et al., 2008) using the Chironico landslide production rate calibration dataset (Claude et al., 2014) and individual ages are reported here using the LSD scaling scheme (Lifton et al., 2014) with one standard deviation ‘external’ uncertainties (see Supplementary Information). From field measurements we applied a topographic shielding correction (Balco et al., 2008), and an erosion rate correction of 1 mm ka^{-1} similar to Schindelwig et al. (2012) and consistent with observations of 0.3–2 cm quartz vein relief on the sampled boulders. To check the consistency of our moraine ages with glacial histories from elsewhere in the region, we re-analysed surface ages from nearby Belalp Glacier (Schindelwig et al., 2012) and Tsidjiore Nouve Glacier (Schimmelpfennig et al., 2012). To determine the age of talus slope 1 (TS1) within the Rothorn cirque, we used a georeferenced orthophoto from 2017 provided by swissTopo (Fig. 5B), historical photos from 1964 (Swissair Photo AG, 1964), 1929 and 1882 (Fig. S2) and LIA moraine deposits (Fig. 1) and reconstructed the deglaciation history of the Hungerli Valley since the LIA (Draebing et al., 2022).

3.2. Recent air and rock temperature measurements

To model permafrost distribution and frost cracking at the rockwalls, air and rock temperature input data were required. For recent frost cracking, a mean annual air temperature (MAAT) for the period 2016–2019 (MAAT_{2016–2019}; Fig. 2), was calculated from data of the nearby meteo station Oberer Stelli Glacier at 2910 m, which has been recording since 2000 (MeteoSwiss, 2022c). As permafrost has a slow response time, a 30-year period is usually applied to model recent permafrost (Boeckli et al., 2012; Magnin et al., 2019). As meteo data from Oberer Stelli glacier was limited to 22 years, we calculated a mean annual air temperature for the 30-year period 1990–2019 (MAAT_{1990–2019}; Fig. 2) from Graechen meteo station. The station is located at a lower elevation (1605 m) than the station at Oberer Stelli Glacier, so a temperature lapse rate of $6\text{ }^{\circ}\text{C km}^{-1}$ was applied to make these records equivalent and appropriate for the Hungerli Valley rockwalls. For rock temperature records, existing data were taken from Draebing et al. (2022) who measured rock surface temperature (RST) at five rockwalls in the Hungerli Valley along an elevation gradient from 2580 to 3148 m (Fig. 1A). Temperatures were measured using Maxim iButton DS1922L loggers installed in 0.1 m deep boreholes in nearly vertical rockwalls (Fig. 2, Table S3). The loggers recorded RST at 3 h intervals (Fig. S3) between 1 September 2016 and 31 August 2019 at RT2 to RT5, and between 29 August 2017 and 28 August 2019 at RT1.

The rockwall thermal regime, and therefore permafrost distribution (Draebing et al., 2017a; Haberkorn et al., 2015), and frost cracking (Anderson et al., 2013; Draebing and Mayer, 2021) are affected by snow cover. To account for this, we used the analysis of Draebing et al. (2022) who examined the daily standard deviation in RST as a measure of snow cover, and applied a uniform threshold of $<0.5\text{ }^{\circ}\text{C}$ for positive and negative RST following established practice (Draebing et al., 2017a; Haberkorn et al., 2015).

3.3. Holocene air and rock temperature reconstructions

For reconstructing paleo frost cracking and permafrost (Fig. 2), we made use of a Younger Dryas (YD) to Little Ice Age (LIA) temperature record from speleothem fluid inclusions from the Milandre cave in Northern Switzerland (Affolter et al., 2019). This record is more suitable for our high elevation site than reconstructions from marine or terrestrial proxies which are seasonally biased by warm temperatures (Samartin et al., 2017). For the Younger Dryas in Europe, reconstructions by Schenk et al. (2018) showed no or only minor summer cooling but seasonality increased resulting in extreme winters with temperatures -11 to $-15\text{ }^{\circ}\text{C}$ colder relative to the Bølling-Allerød period, and increased snow depths. As we aimed to model permafrost and frost cracking, both affected by winter temperatures, we selected a paleo temperature record that reflected winter cooling effects.

Affolter et al. (2019) fitted speleothem fluid inclusions to a Mean Annual Air Temperature (MAAT) data series of Fahey meteo station located at 596 m to convert temperature proxies to temperature values. The reported uncertainty from the transfer function is ± 0.21 to $\pm 0.35\text{ }^{\circ}\text{C}$ for 84 % of the data set. The uncertainties resulting from the temperature transfer function are more than one order of magnitude

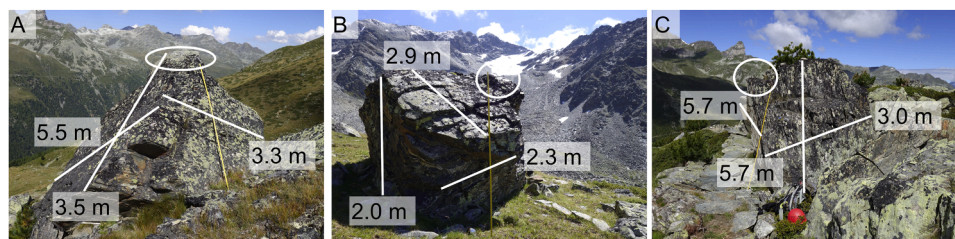


Fig. 3. Examples of sampled boulders with (A) Mo-1 and (B) Mo-6 located at the moraine ridge and (C) Mo-7 located at the ridge of the recessional moraine.

smaller than the differences between paleo and present-day temperatures in the record (Table S2).

To adjust MAAT from low-elevation Switzerland to our high-elevation study area, we derived a temperature lapse rate between meteo stations Oberer Stelli Glacier at 2910 m (MeteoSwiss, 2022c) and Fahey (MeteoSwiss, 2022a) of $4.9 \text{ }^\circ\text{C km}^{-1}$. This temperature adjustment was applied to the reconstructed MAAT from Northern Switzerland to derive a reconstructed air temperature ($\text{MAAT}_{\text{paleo}}$) for our study site. We do not account for complex topography and induced micro-climatic conditions which means the temperature lapse rate approach is only approximate, but as our objective is to compare changes through time, it is probably adequate.

As temperature reconstructions by Affolter et al. (2019) include the beginning of the LIA, and instrumented temperature records are available from 1860 on, we calculated the mean annual air temperature for the Little Ice Age as an average between the paleo temperature records (Affolter et al., 2019) and instrumented temperature records from Grächen (MeteoSwiss, 2022b), both lapse-rate adjusted to 2910 m. We calculated the difference between present day climate ($\text{MAAT}_{1990-2019}$) and paleo climate MAAT and used the differences for permafrost modelling (Table S2, see Section 3.4). As frost-cracking is affected by the near-surface temperature regime, we calculated the difference between present day air temperatures ($\text{MAAT}_{2016-2019}$) and $\text{MAAT}_{\text{paleo}}$. We used this value to correct rock temperatures recorded in 3 h intervals ($\text{RST}_{\text{paleo}}$; Table S3). As measured (present-day) Rock Surface Temperature (RST) is influenced by the presence of seasonal rockwall snow cover, our reconstructed $\text{RST}_{\text{paleo}}$ inherits the influence of this present-day snow cover in the relationship between MAAT and RST. Due to potentially different snow conditions in the past, this inherited relationship may have changed over time. As there exists no method to reliably account for changes in past snow cover for $\text{RST}_{\text{paleo}}$ reconstructions, this remains an uncertainty in our models. Given the steepness of the rockwalls, with limited ability for them to sustain thick snow cover, the paleo snow cover, and therefore the MAAT-RST relationship, is unlikely to have differed much.

3.4. Rock permafrost modelling

Modelling of permafrost at the Hungerli Valley rockwalls was driven by the reconstructed air and rock temperature data, and additional solar radiation simulations. Potential incoming solar radiation (PISR) was simulated for each 2 m digital elevation model (DEM) raster cell using the area solar calculator of ESRI ArcGIS 10.7.1 for the average snow-free period between 2000 and 2019 observed by the meteo station Oberer Stelli Glacier (MeteoSwiss, 2022c) from June to October in hourly steps excluding diffusive solar radiation (Boeckli et al., 2012; Hipp et al., 2014; Magnin et al., 2019). To model the recent rock permafrost distribution in the Hungerli Valley, Draebing et al. (2022) established a multiple linear regression model fitted with multi-annual rock surface temperature (RST) from our temperature loggers and additional south-facing loggers (Table S4), potential incoming solar radiation (PISR) and MAAT following the approach by Magnin et al. (2019):

$$\text{MARST}_{\text{pred}} = a + \text{PISR} * b + \text{MAAT} * c \quad (1)$$

Here a , b and c represent calculated coefficients used to predict mean annual rock surface temperature ($\text{MARST}_{\text{pred}}$). An overall r^2 of 0.94 with a significance value of 0.001 were achieved (Table S5). We interpret a modelled MARST of $<0 \text{ }^\circ\text{C}$ as permafrost (Kenner et al., 2019). We applied the $\text{MAAT}_{1990-2016}$ to Eq. (1) to incorporate the slow response time of rock permafrost into the modelling (Boeckli et al., 2012; Magnin et al., 2019). In this paper, we applied $\text{MAAT}_{\text{paleo}}$ to model past permafrost distribution, thereby, we assume that snow cover duration and PISR was not significantly different. As $\text{MAAT}_{\text{paleo}}$ were lower than today, snow cover was likely to be enhanced in the past (Schenk et al., 2018), and that would reduce PISR. However, the effect of snow cover on RST depends on the timing and duration of snow cover (Draebing

et al., 2017a; Haberkorn et al., 2015). Early thin snow cover can enhance rockwall cooling (Haberkorn et al., 2015), while thick snow cover can prevent cooling (Luetsch et al., 2008). Snow cover late into the warmer months can delay rockwall warming (Draebing et al., 2017a; Haberkorn et al., 2015). Therefore, through changes in the PISR and thermal effects, snow cover can have a positive or negative effect on permafrost distribution. While we cannot completely account for these snow cover effects in our models, we do not believe it will have significantly affected the permafrost model results. The steep rockwalls cannot sustain thick snow mantles, so the effect of snow is probably small compared to the effect of the changing air temperatures. A further source of uncertainty in our permafrost modelling arises from the fact that $\text{MARST}_{\text{pred}}$ neglects complex mountain topography that can influence permafrost distribution due to topographic induced heat transfer (Noetzli et al., 2007), for example from south- to north-facing rockwalls. While this may influence the spatial pattern of permafrost, topographic effects are unlikely to have changed substantially through time, so are unlikely to have affected changes in permafrost through time in the Hungerli Valley.

3.5. Frost cracking modelling

To model frost cracking, we applied the frost cracking model by Rempel et al. (2016) for present (Draebing et al., 2022) and paleo temperature conditions. In the model, frost cracking is presented as increases (% change) in bedrock fracture porosity, driven by pressure gradients from the transport of water towards colder regions of a rock mass (Rempel et al., 2016). The model can incorporate rock strength (fracture toughness), which more realistically accounts for differences in the sensitivity of different rock types to frost cracking, compared to models that use a fixed frost cracking temperature range (Anderson et al., 2013; Hales and Roering, 2007). For our study, we adopted laboratory strength test data from samples from the Hungerli Valley (Draebing et al., 2022). We also incorporated RST (Draebing and Mayer, 2021) instead of using air temperature as a proxy to drive the model, to incorporate the effects of snow cover on frost cracking processes in the present-day climate. With no existing approaches to do so, like for the permafrost modelling, we could not account for differences in snow cover through time when extending the RST time series to the entire Holocene, even though snow cover may have been enhanced in the past (Schenk et al., 2018). As with permafrost modelling, failing to account for snow cover (and complex topography) effects may mean that the magnitude of the intensity changes may not be accurately modelled, but the overall patterns are likely to be realistic.

We propagated measured RST and paleo RSTs into the rockwalls by conductive heat transfer with latent heat effects at the phase transition between water and ice (Anderson et al., 2013; Draebing and Mayer, 2021; see Supporting Information for details). We applied the adjusted and reconstructed rock temperatures to the frost cracking model. The frost cracking model determines an upper temperature limit ΔT_c for segregation ice growth depending on rock strength:

$$\Delta T_c \approx \frac{T_m P_c}{\rho_i L} \text{ with } P_c = \frac{\sqrt{\pi} K_C}{2 \sqrt{x_i}} \quad (2)$$

where T_m is the bulk melting temperature, ρ_i ice density, L latent heat, P_c the critical ice pressure, K_C the critical fracture toughness, and x_i the crack radius. We applied an initial crack length of 0.1 m ($2 * x_i$) and different rock types (strengths) present in the catchment, including the dominant weaker schisty quartz slate, and stronger aplite bands found only in the Rothorn cirque, and bands of amphibolite and aplite in the Hungerli valley (Fig. S5), which resulted in an upper limit of frost cracking between $-2.5 \text{ }^\circ\text{C}$ for amphibolite to $-1.9 \text{ }^\circ\text{C}$ for schist quartz slate. Model results with an initial crack length of 0.1 m reflected best measured fracture densities (Draebing and Mayer, 2021). All model parameters are given in Table S6.

The lower limit of ice segregation is controlled by water availability,

which is determined by permeability:

$$k_{pf} = k_{p0} \left(\frac{\Delta T_f}{\Delta T} \right)^\alpha \quad (3)$$

where k_{pf} is the frozen and k_{p0} the unfrozen permeability, ΔT_f is the pore freezing point, α is a power law exponent, and ΔT is the temperature below the bulk freezing point. We set α to 4 as recommended by Rempel et al. (2016). Water migration in the frozen fringe was calculated based on the unfrozen permeability of the rock mass, with a value of 10^{-18} m^2 adopted for all rockwalls. Permeability is likely heterogeneous within a single rockwall, and will vary slightly between lithologies, however, we consider it reasonable to assume a uniform value, consistent with existing model approaches (e.g. Rempel et al., 2016).

To analyse the dependence of frost cracking on elevation, we calculated the total amount of permanent rock expansion (λ) induced by frost cracking at each rockwall (Rempel et al., 2016). Total rock expansion is a sum of the frost cracking intensity at different depths within the rockwall and is calculated here as:

$$\lambda = \frac{D}{\Delta T_c} \int_1^{\text{year}} \left[\left(\frac{\Delta T_c}{\Delta T} \right)^\alpha \Big|_{z^+, \Delta T \geq \Delta T_c} - \left(\frac{\Delta T_c}{\Delta T} \right)^\alpha \frac{\partial T}{\partial z} \Big|_{z^-, \Delta T \geq \Delta T_c} \right] dt \quad (4)$$

The diffusivity D is

$$D = \frac{\alpha \rho L k_{pf} \Delta T_c}{T_m \mu} \quad (5)$$

where α is a power law exponent and μ is the water viscosity (Rempel et al., 2016). Diffusivity is used as a measure of the propensity for frost-induced porosity changes. Finally, we calculated the mean, lower, and upper range of depth-integrated frost cracking for rock temperature loggers (Fig. S13). We consider the total rock expansion to represent the amount of (depth-integrated) frost cracking taking place at each rockwall.

3.6. Rockwall erosion

To compare recent and paleo rockwall erosion rates, we studied four rockwalls (RW1–4) that have talus slopes (TS1–4) at their base. Draebing et al. (2022) derived a rockfall inventory for 2016–2019 based on annually laserscanning campaigns. Detailed information on data processing is available in the Supplementary Information. In this paper, we used the quantified rockfall volumes to calculate rockwall erosion rates for RW1–4. We quantified the rockwall area A_r of each rockwall (RW1–4) contributing rockfall sediment to the talus slopes (TS1–4) below and calculated the present-day rockwall erosion rate E_r :

$$E_r = \frac{\sum V_r}{A_r t_r} \quad (6)$$

where V_r is the rockfall volume released from the investigate rockwall and t_r is the time between the first and last scan (3 years). In our calculation, we included an assumed uncertainty of rockwall area of 5 %.

We used the talus slopes (TS1–4) below each rockwall (RW1–4) in combination with moraine ages from cosmogenic nuclides to evaluate paleo rates of rockfall activity. None of the selected talus slopes have been reworked by rock glaciers, so that they contain a complete record of rockwall erosion since deglaciation. For three of these talus slopes (named TS1, 2, and 4 in this study), Draebing et al. (2022) had previously evaluated the talus slope volume, by applying electric resistivity tomography (ERT) and seismic refraction tomography (SRT) in longitudinal transects from the rockwall to the toe of three talus slopes. For talus slopes 2 and 4, Draebing et al. (2022) calculated two volumes because of the possible presence of basal moraine, which, if present, would result in a smaller talus volume. A fourth talus slope (TS3) was investigated by Otto and Sass (2006) by applying ERT, SRT and ground

penetrating radar (GPR). They detected a potential basal moraine at similar depths to Draebing et al. (2022). We assume an uncertainty of 5 % in our talus slope volume V_t calculation. We re-calculated the paleo rockwall erosion E_t as:

$$E_t = V_t \frac{\rho_r}{\rho_r A_r t} \quad (7)$$

where ρ_r is the density of the rockwall (2800 kg m^{-3}), ρ_t is talus density, and t is the time period of talus accumulation. Talus density varies vertically from 2000 kg m^{-3} near the surface to 2500 kg m^{-3} at the base (Scapozza et al., 2015). We incorporated the entire range of talus density into our erosion rate calculation to avoid bias from densification (sensu Sadler, 1981) if using only a single value. The time period of talus accumulation (t) was derived from historic photos for TS1 (55 a; Draebing et al., 2022) and for TS2–4 from the cosmogenic nuclide exposure age dating of nearby moraines presented in this study. We assume that talus slope accumulation commenced once the glacier had retreated up-valley of each rockwall (i.e., while the glacier was present, rockfall debris would be transported away from the base of the rockwall by the glacier). As TS2–4 are located between the recessional moraine ridge and the rockwalls (Fig. 1) with a mean age of $10.0 \pm 0.2 \text{ ka}$ ($n = 3$) and individual boulder age between 9.8 ± 0.7 and $10.2 \pm 0.7 \text{ ka}$, we assume that the maximum talus slope age ranges between 9 and 10 ka. We applied this range to the erosion rate calculation.

We collated published paleo rockwall erosion rates (Table S8) from other study sites within the European Alps for which recent rockwall erosion rates (Table S7) were also available, to compare against the rates measured in this study for the Hungerli Valley.

4. Results

4.1. Glacier retreat history and rockwall deglaciation

Our reconstructions of the Rothorn Glacier suggest that the studied rockwalls have been mostly glacier-free during the Holocene. The age of the outer moraine ridge ($11.0 \pm 0.6 \text{ ka}$, Figs. 4D and 6) corresponds to the climate transition between the YD and early Holocene, and was synchronous with the nearby Tsidjiore Nouve Glacier moraine ridges ($10.9 \pm 0.3 \text{ ka}$ and $10.8 \pm 0.2 \text{ ka}$) (Fig. 4C; Schimmelpfennig et al., 2012). The inner recessional ridge ($10.0 \pm 0.2 \text{ ka}$) accords with the transition to warmer conditions of the HTM, and was synchronous with the outermost moraine of the nearby Belalp Glacier ($10.1 \pm 0.2 \text{ ka}$, Fig. 4B; Schindelwig et al., 2012).

The three lower rockwalls (RW2–4) were glacier covered below 2700 m elevation during the LGM, while ice was present at between 2580 and 2680 m during the subsequent YD advance (Figs. 5 and 7). RW2–4 have therefore been glacier-free since $\sim 10 \text{ ka}$, and talus accumulation below the rockwalls would have begun no earlier than 10 ka, after the glacier retreated from the YD limits (Fig. 6). This is corroborated by the identification, in geophysical surveys, of a moraine beneath the talus (Draebing et al., 2022; Otto and Sass, 2006). The uppermost rockwall (RW1) became ice-free between 1929 and 1964, with talus accumulation since 1964 (Fig. 5).

4.2. Temperature reconstructions

Meteo station records revealed a MAAT_{2016–19} at 2910 m of -0.9°C , 0.8°C warmer (Table S2), than the 30-year average (MAAT_{1990–2019}, -1.7°C). During YD MAAT was $-11.3^{+2.0}_{-3.3} \text{C}$ (Fig. 4A). The temperature increased during the HTM to $-2.7^{+0.2}_{-0.4} \text{C}$, however, temperature fluctuated with a warmest peak during the HTM of $-1.5^{+0.1}_{-0.1} \text{C}$ and a cold spell at 8.2 ka BP of $-4.4^{+0.5}_{-0.9} \text{C}$. The period between HTM and LIA showed an average temperature of $-3.0^{+0.2}_{-0.4} \text{C}$, while temperatures during LIA decreased to $-3.7^{+0.5}_{-0.5} \text{C}$.

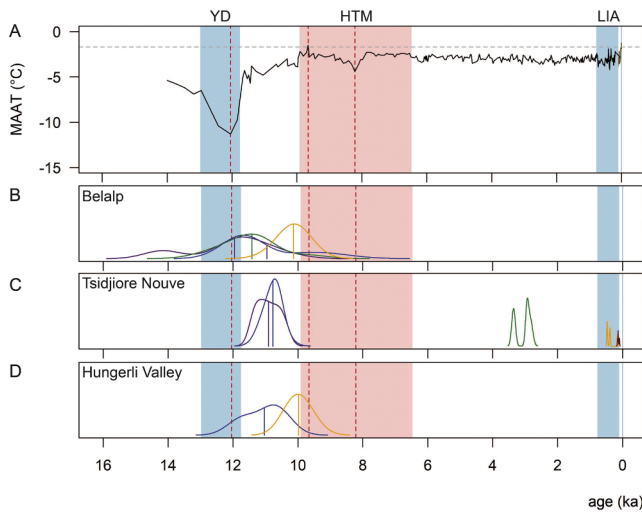


Fig. 4. (A) Reconstructed mean annual air temperatures (MAAT; black line) from the Milandre cave (Affolter et al., 2019) and measured MAAT (brown line) from the meteo station Grächen for 1864 to 2019 (MeteoSwiss, 2022b) adjusted to an elevation of 2910 m. Moraine ages recalculated to be consistent with LSD scaling for (B) the Belalp Glacier (Schindelwig et al., 2012); (C) Tsidjiore Nouve Glacier (Schimmelpennig et al., 2012); and (D) Rothorn Glacier in the Hungerli Valley. Lines represent summed probability curves with vertical lines represent arithmetic means. Colours highlight the stratigraphical order of moraines (from outer moraine to LIA) for each location. Blue shading highlights cold phases as the Younger Dryas (YD) and the Little Ice Age (LIA), while red shading highlights the Holocene Thermal Maximum (HTM). Red dotted lines highlight key model time steps; the YD minima (~12 ka BP), the warm HTM peak at 9.6 ka BP, and the HTM cold spell at 8.2 ka BP. (For interpretation of the references to color in this figure legend, the reader is referred to the web version of this article.)

4.3. Permafrost and frost cracking patterns

During the cold phase of the YD all the studied rockwalls were affected by permafrost (Fig. 7C, Fig. S4). In the following, we use the term permafrost aggradation for an increase of areal extent and permafrost degradation for a decrease. The warming that followed until 9.6 ka BP resulted in permafrost degradation of 20–80 % for elevation

bands below 3100 m (Fig. 7). During the 8.2 ka HTM cold phase, permafrost aggraded at all rockwalls (Fig. 7F), but on average during the HTM, rockwalls below 3000 m experienced permafrost degradation of 10–40 % relative to the YD (Fig. 7E). Subsequent cooling restricted permafrost-free conditions to only 10–30 % of the rockwall area below 2900 m (Fig. 7G), with further aggradation during the LIA leaving little rockwall area below 2700 m free from permafrost (Fig. 7H). Thawing between the LIA and present-day, reduced permafrost by 20–100% for elevations below 3100 m (Fig. 7I).

Our models suggest that maximum frost cracking during the YD occurred at an elevation of 2700 m (Fig. 7C). With warming until 9.6 ka BP, frost cracking intensity decreased at all elevations, with maximum intensity rising to 2930 m (Fig. 7D). The cooling period at 8.2 ka BP intensified frost cracking, with elevation of maximum intensity differing between lithologies (Fig. 7F). The maximum for schisty quartz slate was located at 2680 m but at 2930 m for aplite and amphibolite. From the HTM to the LIA, frost cracking intensified at each elevation, with a maximum at 2930 m (Fig. 7E, G-H). This elevation pattern persisted to the present-day, but with decreased intensities at all elevations (Fig. 7I).

4.4. Rockwall erosion rates

Laserscanning surveys between 2016 and 2019 identified 38 rock-

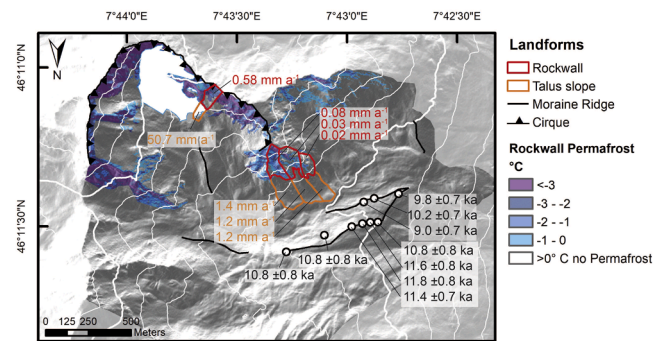


Fig. 6. Modelled recent Mean Annual Rock Surface Temperature (MARST), reconstructed moraine ages and quantified paleo erosion rates derived from talus slopes and recent erosion rates derived from rockwalls (source: swissALTI3d from swissTopo). A MARST below 0 °C is interpreted as rock permafrost.

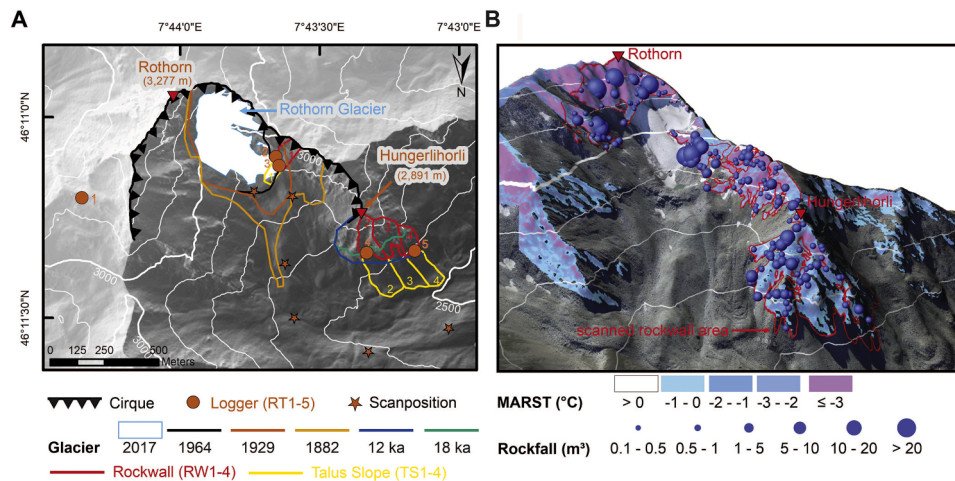


Fig. 5. Rockfall events along with glacier history, permafrost distribution and talus slopes in the Hungerli Valley. (A) Investigated rockwalls (RW1–4, red polygons) above investigated talus slopes (TS1–2, yellow polygons) in the Hungerli Valley, with highlighted glacier history (coloured lines), rock temperature loggers (RT1–5, orange points), and scan positions (orange stars) (source: swissALTI3d from swissTopo). (B) 3D representation of all scanned rockwall areas (red rectangle), modelled permafrost distribution and quantified rockfall volumes for 2016 to 2019 for all north-facing rockwalls in the catchment (source: swissALTI3d and swissIMAGE25 from swissTopo). Figure reproduced from Draebing et al. (2022). (For interpretation of the references to color in this figure legend, the reader is referred to the web version of this article.)

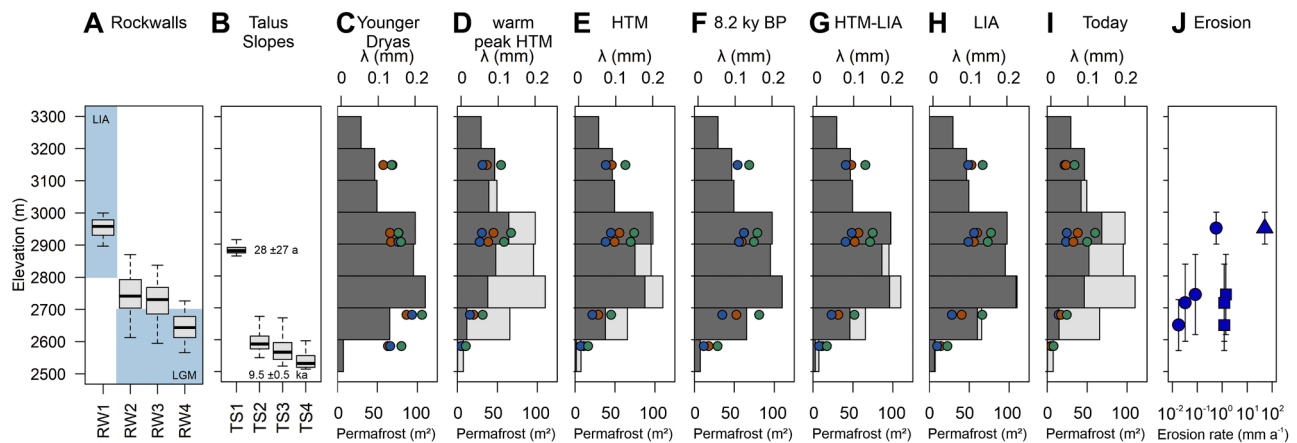


Fig. 7. (A) Elevations of the four studied rockwalls of Hungerli Valley, with blue rectangles showing the glacier ice distribution at the LIA (RW1) and LGM (RW2–4). (B) Talus slope elevations, with the integration age labelled. (C–I) Hypsometry of current rockwalls (light grey bars) and permafrost affected rockwalls (dark grey bars), and modelled frost cracking (coloured dots as λ in mm) for each lithology (amphibolite = blue, aplite = red, schisty quartz slate = green), for each modelled timestep. (J) Rockwall erosion rates for the present-day (circles), decadal (triangles), and Holocene (rectangles). (For interpretation of the references to color in this figure legend, the reader is referred to the web version of this article.)

falls, producing erosion rates of $0.02\text{--}0.58\text{ mm a}^{-1}$ at the four rockwalls (Table 1, Fig. 6). Thirteen of these rockfalls occurred at RW1, with volumes of between 0.1 and 3.5 m^3 , equating to an erosion rate of $0.58^{+0.01}_{-0.01}\text{ mm a}^{-1}$. Fourteen rockfalls from RW2, with volumes of $0.1\text{--}3.2\text{ m}^3$, equate to an erosion rate of $0.08^{+0.00}_{-0.00}\text{ mm a}^{-1}$. Nine rockfalls occurred at RW3, with volumes of $0.1\text{--}0.6\text{ m}^3$, giving an erosion rate of $0.03^{+0.00}_{-0.00}\text{ mm a}^{-1}$. Only two rockfalls, with volumes of 0.1 and 0.6 m^3 , occurred at RW4, producing an erosion rate of $0.02^{+0.00}_{-0.00}\text{ mm a}^{-1}$. The long-term (Holocene or last $\sim 10\text{ ka}$) erosion rates, calculated from the three lower talus slopes ranged from $1.2^{+0.6}_{-0.4}\text{ mm a}^{-1}$ to $1.4^{+0.6}_{-0.5}\text{ mm a}^{-1}$ (Fig. 6, Table 1). TS1, which has been accumulating for the last 55 years, adjacent to the retreating Rothorn Glacier, gave a medium-term (decadal) erosion rate of $50.7^{+10.9}_{-10.3}\text{ mm a}^{-1}$, two orders of magnitude higher than the recent (2016–2019) rate for this rockwall.

5. Discussion

5.1. Paleo versus recent rockwall erosion rates in the Hungerli Valley

The paleo rates of rockwall erosion exceed the recent rates in the Hungerli Valley by two orders of magnitude. Before discussing the processes behind this, we briefly consider whether this finding is by chance alone because our window of observation (of three years) was too short to capture natural variability, or because our paleo rates have been overestimated. Erosion rates are sensitive to the time scale of observation (Gardner et al., 1987; Guerin et al., 2020) especially so in

Table 1
Reconstructed rockwall erosion rates in the Hungerli Valley.

Location	Elevation (m)	Rockwall erosion rate (mm a^{-1})	Integration Time (a)
<i>Recent (2016–2019) rates</i>			
RW1	2949 ± 51	$0.58^{+0.01}_{-0.01}$	3
RW2	2742 ± 126	$0.08^{+0.00}_{-0.00}$	3
RW3	2716 ± 121	$0.03^{+0.00}_{-0.00}$	3
RW4	2646 ± 80	$0.02^{+0.00}_{-0.00}$	3
<i>'Paleo' (decadal) rates</i>			
RW1	2949 ± 51	$50.7^{+10.9}_{-10.3}$	55
<i>Paleo (Holocene) rates</i>			
RW2	2742 ± 126	$1.4^{+0.6}_{-0.5}$	9500 ± 500
RW3	2716 ± 121	$1.2^{+0.2}_{-0.2}$	9500 ± 500
RW4	2646 ± 80	$1.2^{+0.6}_{-0.4}$	9500 ± 500

mountain settings where erosion is episodic (Kirchner et al., 2001). Measurements of short-term erosion rates can be biased by the presence or absence of low-frequency, high magnitude events within the monitoring window (Guerin et al., 2020). We believe our 3-year monitoring window is representative of recent erosion. Climate has been warming over the past few decades, and the climate during the period 2016–2019 fits with this trend and was not an anomalously quiet period in terms of potential rockfall-triggering weather events. Based on the rock mass conditions it is unlikely that we have under-represented high magnitude rockfalls. Rockfall volume is limited by fracture spacing (de Vilder et al., 2017; Verdian et al., 2021), and the fracture spacing at the Hungerli Valley rockwalls is small, with RW 1, 2 and 4 having an average spacing of between 0.12 and 1.16 m (Draebing and Mayer, 2021). Consequently, fracture spacing in our area suggests a geologic control that would tend to produce smaller rockfall volumes, with rockwalls that are more likely to erode by multiple small, frequent events than by infrequent larger-scale single rockfalls or multiblock rockfalls (Williams et al., 2019). The rockfall volumes measured on the entire north-facing rockwall revealed volumes from 0.1 to 159.4 m^3 , a medium volume of 0.26 m^3 , and 96% smaller than 10 m^3 (Draebing et al., 2022). The magnitude-frequency relationship is typical for landslides, without any indication that the frequency of larger events during the 2016–2019 period was unusually low (Fig. S14).

Paleo erosion rates for the Holocene or longer periods integrate short-lived episodes of higher-than-average erosion (e.g. Kirchner et al., 2001) resulting from exemplary glacier retreat (e.g. Hinchliffe and Ballantyne, 1999) and periods of lower-than-average erosion into one averaged erosion rate. Previous studies showed a high temporal variability of erosion within averaged periods (e.g. Grischott et al., 2017; Hinchliffe and Ballantyne, 1999), which we cannot resolve from our rockfall reconstruction based on talus slopes. Postglacial erosion derived from sedimentary archives can be biased by stratigraphic incompleteness or densification (Sadler, 1981) and sediment dynamics (Jerolmack and Paola, 2010). These (Sadler) effects usually lead to under- rather than over-estimation, of long-term sedimentation rates. Nonetheless, we incorporated uncertainty related to these effects into our measurements. We incorporated uncertainty related to talus density, by applying a conservative range of 2000 to 2500 kg m^{-3} according to a previous study (Scapozza et al., 2015). To measure the talus thickness, we re-analysed geophysical data used to differentiate talus deposits from sub-surface moraine material (Draebing et al., 2022; Otto and Sass, 2006), and included 5% uncertainty in the talus volume and contributing rockwall area. Moreover, the talus accumulations in the Hungerli Valley

are unlikely to have been significantly affected by processes of erosion, densification, or other alteration. The valley has been disconnected from the main trunk valley throughout the Holocene (Otto et al., 2009) and there is no morphological evidence that the talus slopes have been affected by rock glacier dynamics. A source of uncertainty for our long-term measurements is whether they contain the effects of rare, large-magnitude earthquakes (e.g. Oswald et al., 2021) or extreme weather events. This is a possibility that we cannot exclude, but even if such events have contributed excessive erosion compared to the recent (2016–2019) rates, they are unlikely to be the sole reason.

Considering these factors outlined above, the two-orders-of-magnitude difference in long-term and recent rates, and the consistent trend of both recent and paleo erosion rates increasing with elevation, we believe that rockwall erosion rates were truly higher in the past compared with the present day. Based on our frost-cracking and permafrost reconstructions, we believe we have identified a suitable mechanism to explain this reduction in erosion through time.

5.2. Drivers of rockwall erosion

5.2.1. A rapid paraglacial response

The highest erosion rate ($50.7^{+10.9}_{-10.3}$ mm a⁻¹) was found from the talus accumulated over the past 55 years below the recently deglaciated RW1 (Fig. 6). This rate dropped to just $0.58^{+0.01}_{-0.01}$ mm a⁻¹ between 2016 and 2019, suggesting a rapidly fading response of small debris and boulder falls ($\leq 10^3$ m³) to the destabilizing effects of deglaciation. This is in accordance with paraglacial models (Augustinus, 1995) and other rockfall monitoring studies (Hartmeyer et al., 2020). It also suggests that rapid responses for small rockwalls differ to the longer (millennial-scale) response times found for major rockslope failures ($\geq 10^6$ m³) from large rockwalls experiencing retreat of major valley glaciers (McColl, 2012). The majority of the rockwall surfaces of RW2–4 have been ice free since the LGM, and any sediments from paraglacial rockfall following the LGM would have been removed by the YD glacier advance. The YD glacier was in contact with the lower part of the rockwall, however, mechanical modelling demonstrated that pure mechanical loading and unloading due to the glacier is not producing sufficient rockwall damage that can lead to paraglacial rockfall (Grämiger et al., 2017). Glacial erosion can increase fracturing of neighbouring rockwalls (Grämiger et al., 2017), however, moraine dimensions and current valley slope angle suggest low ice thickness and ice surface slope for the YD glacier which reduces sliding velocity and glacial erosion (Herman et al., 2021). Therefore, we conclude that paraglacial effects on talus slopes TS2–4 were unlikely. Alternatively, studies suggest pronounced talus slope accumulations by enhanced rockfall activity under periglacial conditions due to frost weathering (Hales and Roering, 2009; Hinchliffe and Ballantyne, 1999) or permafrost (Ravel and Deline, 2010).

5.2.2. Rock permafrost and frost cracking

Our Holocene reconstructions suggest that both permafrost aggradation and degradation (increase and decrease of areal extent) occurred, both of which can drive rockwall erosion (Krautblatter et al., 2013; Matthews et al., 2018; Ravel and Deline, 2010). Permafrost degradation occurred at rockwalls between 2500 and 3100 m after the YD and LIA, and less so at rockwalls between 2500 and 2900 m after the 8.2 ka HTM cold spell (Fig. 7D, G, I). Permafrost degradation may partly explain the high erosion rates measured at the high elevation RW1 over the 55-years since 1964, and in the Holocene at TS2–4 which integrate three periods of warming. Permafrost aggradation occurred during the cold spell 8.2 ka BP at elevations between 2500 and 3000 m (Fig. 7F) and during LIA at elevations between 2500 and 2900 m (Fig. 7H).

The other key process to explain higher Holocene erosion rates is higher frost cracking intensities. Our frost cracking models suggest RW2–4 experienced greater frost cracking intensities in several periods of the Holocene relative to the present. Colder periods such as YD, the

cold spell at 8.2 ka BP and LIA significantly increased the frost cracking magnitude at RW2–4 (Fig. 7C, F, H) as rock temperatures were below the upper limit of frost cracking between -2.5 °C for amphibolite to -1.9 °C for schist quartz slate. At elevations above 2900 m (RW1 and higher), rock temperatures were below the upper frost cracking window in temperature range that favoured frost cracking (Fig. 7C–H). Only under present conditions have rock temperatures increased sufficiently to decrease the frost cracking magnitude (Fig. 7I).

Although we have not accounted for snow cover variability (Draebing et al., 2017a; Haberkorn et al., 2015) and changes in the MARST from topographic induced heat transfer (Noetzi et al., 2007) over the Holocene, these effects are likely to have changed the magnitudes of permafrost change and frost cracking intensities, but not the overall pattern. Changes in permafrost during the Holocene, and increases in frost cracking intensities, will have accelerated rockwall erosion in the Hungerli Valley. While we are unable to quantify how much rockwall erosion will have changed as a result, these processes provide plausible explanations for why Holocene erosion rates exceed the recent rates.

5.3. The discrepancy between recent and paleo rockwall erosion in the European Alps

Our findings provide support for previous studies that have also found paleo rockwall erosion rates exceeded recent erosion rates. If applicable beyond the Hungerli Valley, our climate reconstructions and modelling of Holocene changes in permafrost and intensified frost weathering may provide an explanation for this regional trend. While direct comparison of our results to rockwalls beyond the Hungerli Valley needs caution if comparing absolute magnitudes due to local differences, the general patterns are transferable. Our models of permafrost and frost cracking patterns suggest climate-induced episodic rockwall erosion during earlier times in the Holocene exceeded those of the present-day in many parts of the European Alps (Fig. 8; Mohadjer et al., 2020; Sass, 2005). Only at the Zugspitze do recent rates exceed past rates, likely due to the combination of intense frost cracking and permafrost thaw (Krautblatter et al., 2010) at that high elevation site (>2900 m). The majority of other investigated sites of a similar dominant lithology (Fig. 8) are below the current permafrost limits (Boeckli et al., 2012), suggesting that rockwalls are adjusted to non-permafrost conditions resulting in reduced present-day rockfall activity. In contrast, permafrost is present at the higher elevation rockwalls of the Hungerli Valley, which may (in addition to unaccounted differences in geology) explain why the recent rockfall rates of RW1 exceed the recent rates found at the lower rockwalls in the Hungerli Valley and elsewhere in the European Alps.

6. Conclusions

In this study, we reconstructed Holocene changes in periglacial processes and associated rockfall in an alpine valley, from the past 10 ka to the present-day (2016–2019). We found that rockwalls deglaciated prior to the Younger Dryas experienced higher average erosion in the past 10 ka compared to the present day. Our models suggest this relates to higher frost cracking intensities and cycles of permafrost aggradation and degradation in the past. For a high-elevation, recently deglaciated rockwall, erosion rates were much greater but decayed rapidly, which we infer to paraglacial adjustment, permafrost thaw and high frost cracking activity. Our findings confirm that climate-driven changes in periglacial processes and permafrost distribution strongly influence the rates and patterns of rockwall erosion at alpine rockwalls, and explain the divergence between paleo and recent rates of rockfall activity in the European Alps.

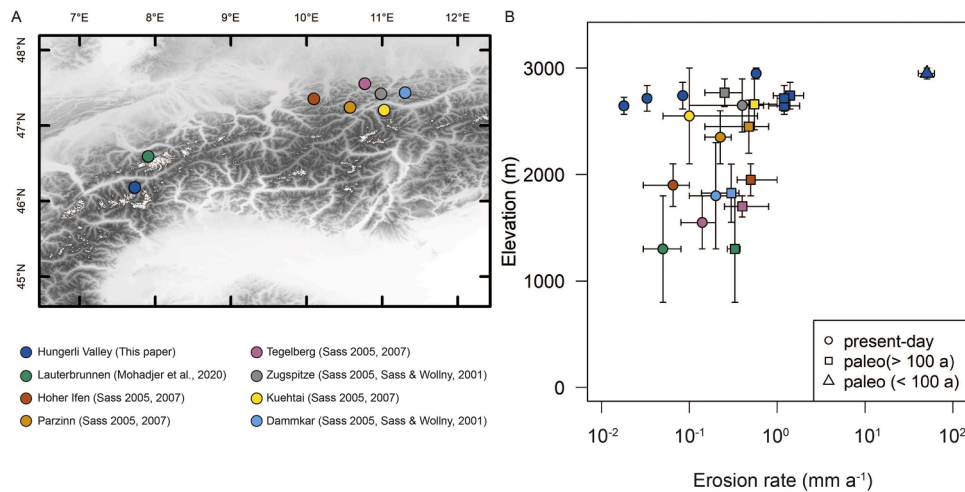


Fig. 8. (A) Location of the areas with recent and paleo erosion rates in the European Alps (DEM source: European Digital Elevation Model) (Sass, 2007; Sass and Wolny, 2001). (B) Comparison of present-day (circles) and paleo erosion rates in relation to elevation, for the Hungerli Valley and selected areas. Paleo rates are shown averaged over Little Ice Age (triangles) and Holocene (rectangles) to present day timescales.

Data availability

The temperature and rockfall data that support the findings of this study are available at figshare (<https://doi.org/10.6084/m9.figshare.17152481.v1>) (Draebing et al., 2021). For the regional analysis, we used freely available data including a 25 m digital elevation model of the European Alps provided by Copernicus (<https://land.copernicus.eu/imagery-in-situ/eu-dem/eu-dem-v1.1>). Digital elevation data (swissALTI3D; <https://www.swisstopo.admin.ch/de/geodata/height/alti3d.html>) and orthophoto (swissIMAGE25; <https://www.swisstopo.admin.ch/de/geodata/images/ortho/swissimage25.html>) is available from swissTopo. Meteo data used in this study is free available from MeteoSwiss (<https://gate.meteoswiss.ch/idaweb>). Cosmogenic nuclide data is available at figshare (<https://doi.org/10.6084/m9.figshare.24581514>) and at the informal cosmogenic-nuclide exposure-age database (www.ice-d.org). Paleo erosion rate data is available in the Supplementary Information.

CRediT authorship contribution statement

Daniel Draebing: Writing – review & editing, Writing – original draft, Visualization, Supervision, Project administration, Methodology, Investigation, Funding acquisition, Formal analysis, Data curation, Conceptualization. **Till Mayer:** Writing – review & editing, Writing – original draft, Software, Methodology, Investigation, Formal analysis. **Benjamin Jacobs:** Writing – review & editing, Writing – original draft, Visualization, Methodology, Investigation, Data curation. **Steven A. Binnie:** Writing – review & editing, Writing – original draft, Methodology, Formal analysis, Data curation. **Miriam Dühnforth:** Methodology, Formal analysis, Conceptualization. **Samuel T. McColl:** Writing – review & editing, Writing – original draft, Investigation, Data curation, Conceptualization.

Declaration of Competing Interest

The authors declare that they have no known competing financial interests or personal relationships that could have appeared to influence the work reported in this paper.

Acknowledgements

We acknowledge the valuable comments by Greg Stock and five anonymous reviewers that improved this manuscript. We also thank the

several students who assisted with fieldwork and sample preparation of ¹⁰Be dating and are grateful to Elena Voronina and Manfred Fischer for laboratory assistance. Funding was provided by the German Research Foundation (DR1070/3–1, 426793773) and MBIE SSIF-funded Hazards Programme at GNS Science (contract C05X1702).

Supplementary materials

Supplementary material associated with this article can be found, in the online version, at [doi:10.1016/j.epsl.2023.118496](https://doi.org/10.1016/j.epsl.2023.118496).

References

- Affolter, S., Häuselmann, A., Fleitmann, D., Edwards, R.L., Cheng, H., Leuenberger, M., 2019. Central Europe temperature constrained by speleothem fluid inclusion water isotopes over the past 14,000 years. *Sci. Adv.* 5 (6), eaav3809. <https://doi.org/10.1126/sciadv.aav3809>.
- Anderson, R.S., Anderson, S.P., Tucker, G.E., 2013. Rock damage and regolith transport by frost: an example of climate modulation of the geomorphology of the critical zone. *Earth Surf. Processes Landforms* 38 (3), 299–316. <https://doi.org/10.1002/esp.3330>.
- Augustinus, P.C., 1995. Glacial valley cross-profile development: the influence of in situ rock stress and rock mass strength, with examples from the Southern Alps, New Zealand. *Geomorphology* 14 (2), 87–97. [https://doi.org/10.1016/0169-555X\(95\)00050-X](https://doi.org/10.1016/0169-555X(95)00050-X).
- Balco, G., Stone, J.O., Lifton, N.A., Dunai, T.J., 2008. A complete and easily accessible means of calculating surface exposure ages or erosion rates from ¹⁰Be and ²⁶Al measurements. *Quat. Geochronol.* 3 (3), 174–195. <https://doi.org/10.1016/j.quageo.2007.12.001>.
- Ballantyne, C.K., Wilson, P., Gheorghiu, D., Rodés, À., 2014. Enhanced rock-slope failure following ice-sheet deglaciation: timing and causes. *Earth Surf. Processes Landforms* 39 (7), 900–913. <https://doi.org/10.1002/esp.3495>.
- Boeckli, L., Brenning, A., Gruber, S., Noetzi, J., 2012. A statistical approach to modelling permafrost distribution in the European Alps or similar mountain ranges. *Cryosphere* 6 (1), 125–140. <https://doi.org/10.5194/tc-6-125-2012>.
- Church, M., Slaymaker, O., 1989. Disequilibrium of holocene sediment yield in glaciated British-Columbia. *Nature* 337 (6206), 452–454. <https://doi.org/10.1038/337452a0>.
- Claude, A., Ivy-Ochs, S., Kober, F., Antognini, M., Salcher, B., Kubik, P.W., 2014. The Chironico landslide (Valle Leventina, southern Swiss Alps): age and evolution. *Swiss J. Geosci.* 107 (2), 273–291. <https://doi.org/10.1007/s00015-014-0170-z>.
- Cook, S.J., Swift, D.A., Kirkbride, M.P., Knight, P.G., Waller, R.I., 2020. The empirical basis for modelling glacial erosion rates. *Nat. Commun.* 11 (1), 759. <https://doi.org/10.1038/s41467-020-14583-8>.
- de Vilder, S.J., Rosser, N.J., Brain, M.J., 2017. Forensic analysis of rockfall scars. *Geomorphology* 295, 202–214. <https://doi.org/10.1016/j.geomorph.2017.07.005>.
- Delunel, R., Schlunegger, F., Valla, P.G., Dixon, J., Glotzbach, C., Hippe, K., Kober, F., Molliex, S., Norton, K.P., Salcher, B., Wittmann, H., Akçar, N., Christl, M., 2020. Late-Pleistocene catchment-wide denudation patterns across the European Alps. *Earth Sci. Rev.* 211, 103407. <https://doi.org/10.1016/j.earscirev.2020.103407>.
- Delunel, R., van der Beek, P.A., Carcaillet, J., Bourles, D.L., Valla, P.G., 2010. Frost-cracking control on catchment denudation rates: insights from in situ produced Be-10 concentrations in stream sediments (Ecrins-Pelvoux massif, French Western Alps).

- Earth Planet. Sci. Lett. 293 (1–2), 72–83. <https://doi.org/10.1016/j.epsl.2010.02.020>.
- Draebing, D., Haberkorn, A., Krautblatter, M., Kenner, R., Phillips, M., 2017a. Thermal and mechanical responses resulting from spatial and temporal snow cover variability in Permafrost Rock Slopes, Steintaelli, Swiss Alps. *Permafrost Periglac. Process.* 28 (1), 140–157. <https://doi.org/10.1002/ppp.1921>.
- Draebing, D., Krautblatter, M., 2019. The efficacy of frost weathering processes in alpine rockwalls. *Geophys. Res. Lett.* 46 (12), 6516–6524. <https://doi.org/10.1029/2019gl081981>.
- Draebing, D., Krautblatter, M., Hoffmann, T., 2017b. Thermo-cryogenic controls of fracture kinematics in permafrost rockwalls. *Geophys. Res. Lett.* 44 (8), 3535–3544. <https://doi.org/10.1002/2016GL072050>.
- Draebing, D., Mayer, T., 2021. Topographic and geologic controls on frost cracking in Alpine rockwalls. *J. Geophys. Res.* 126 (6), e2021JF006163 <https://doi.org/10.1029/2021JF006163>.
- [dataset] Draebing, D., Mayer, T., Jacobs, B., McColl, S.T., 2021. Alpine rockwall erosion patterns follow elevation-dependent climate trajectories. *Figshare*. <https://doi.org/10.6084/m9.figshare.17152481.v1>.
- Draebing, D., Mayer, T., Jacobs, B., McColl, S.T., 2022. Alpine rockwall erosion patterns follow elevation-dependent climate trajectories. *Commun. Earth Environ.* 3 (1), 21. <https://doi.org/10.1038/s43247-022-00348-2>.
- Fryirs, K.A., Brierley, G.J., Preston, N.J., Kasai, M., 2007. Buffers, barriers and blankets: the (dis)connectivity of catchment-scale sediment cascades. *Catena* 70 (1), 49–67. <https://doi.org/10.1016/j.catena.2006.07.007>.
- Gardner, T.W., Jorgensen, D.W., Shuman, C., Lemieux, C.R., 1987. Geomorphic and tectonic process rates: effects of measured time interval. *Geology* 15 (3), 259–261. [https://doi.org/10.1130/0091-7613\(1987\)15<259:Gatpre>2.0.Co;2](https://doi.org/10.1130/0091-7613(1987)15<259:Gatpre>2.0.Co;2).
- Grämiger, L.M., Moore, J.R., Gischig, V.S., Ivy-Ochs, S., Loew, S., 2017. Beyond debuttressing: mechanics of paraglacial rock slope damage during repeat glacial cycles. *J. Geophys. Res.* 122 (4), 1004–1036. <https://doi.org/10.1002/2016JF003967>.
- Grischott, R., Kober, F., Lupker, M., Reitner, J.M., Drescher-Schneider, R., Hajdas, I., Christl, M., Willett, S.D., 2017. Millennial scale variability of denudation rates for the last 15 kyr inferred from the detrital ¹⁰Be record of Lake Stappitz in the Hohe Tauern massif, Austrian Alps. *Holocene* 27 (12), 1914–1927. <https://doi.org/10.1177/0959683617708451>.
- Guerin, A., Stock, G.M., Radue, M.J., Jaboyedoff, M., Collins, B.D., Matasci, B., Avdievitch, N., Derron, M.-H., 2020. Quantifying 40 years of rockfall activity in Yosemite Valley with historical Structure-from-Motion photogrammetry and terrestrial laser scanning. *Geomorphology* 356, 107069. <https://doi.org/10.1016/j.geomorph.2020.107069>.
- Haberkorn, A., Phillips, M., Kenner, R., Rhyner, H., Bavay, M., Galos, S.P., Hoelzle, M., 2015. Thermal regime of rock and its relation to snow cover in steep alpine rock walls: gemsstock, Central Swiss Alps. *Geografiska Annaler* 97 (3), 579–597. <https://doi.org/10.1111/geoa.12101>.
- Hales, T.C., Roering, J.J., 2007. Climatic controls on frost cracking and implications for the evolution of bedrock landscapes. *J. Geophys. Res.-Earth Surf.* 112, F02033. <https://doi.org/10.1029/2006jf000616>.
- Hales, T.C., Roering, J.J., 2009. A frost "buzzsaw" mechanism for erosion of the eastern Southern Alps, New Zealand. *Geomorphology* 107 (3–4), 241–253. <https://doi.org/10.1016/j.geomorph.2008.12.012>.
- Hartmeyer, I., Delleske, R., Keuschnig, M., Krautblatter, M., Lang, A., Schrott, L., Otto, J. C., 2020. Current glacier recession causes significant rockfall increase: the immediate paraglacial response of deglaciating cirque walls. *Earth Surf. Dyn.* 8 (3), 729–751. <https://doi.org/10.5194/esurf-8-729-2020>.
- Herman, F., De Doncker, F., Delaney, I., Prasicek, G., Koppes, M., 2021. The impact of glaciers on mountain erosion. *Nat. Rev. Earth Environ.* 2 (6), 422–435. <https://doi.org/10.1038/s43017-021-00165-9>.
- Hinchliffe, S., Ballantyne, C.K., 1999. Talus accumulation and rockwall retreat, Trotternish, Isle of Skye, Scotland. *Scott. Geographic. J.* 115 (1), 53–70. <https://doi.org/10.1080/00369229918737057>.
- Hinderer, M., Kastowski, M., Kamelger, A., Bartolini, C., Schlunegger, F., 2013. River loads and modern denudation of the Alps — a review. *Earth Sci. Rev.* 118, 11–44. <https://doi.org/10.1016/j.earscirev.2013.01.001>.
- Hipp, T., Eitzel, B., Westermann, S., 2014. Permafrost in Alpine Rock Faces from Jotunheimen and Hurrungane, Southern Norway. *Permafrost Periglacial Process.* 25 (1), 1–13. <https://doi.org/10.1002/ppp.1799>.
- Jerolmack, D.J., Paola, C., 2010. Shredding of environmental signals by sediment transport. *Geophys. Res. Lett.* 37 (19) <https://doi.org/10.1029/2010GL044638>.
- Kelly, M.A., Buoncristiani, J.F., Schlüchter, C., 2004. A reconstruction of the last glacial maximum (LGM) ice-surface geometry in the western Swiss Alps and contiguous Alpine regions in Italy and France. *Ecol. Geol.* 97 (1), 57–75. <https://doi.org/10.1007/s00015-004-1109-6>.
- Kenner, R., Noetzi, J., Hoelzle, M., Raetz, H., Phillips, M., 2019. Distinguishing ice-rich and ice-poor permafrost to map ground temperatures and ground ice occurrence in the Swiss Alps. *Cryosphere* 13 (7), 1925–1941. <https://doi.org/10.5194/tc-13-1925-2019>.
- Kirchner, J.W., Finkel, R.C., Riebe, C.S., Granger, D.E., Clayton, J.L., King, J.G., Megahan, W.F., 2001. Mountain erosion over 10yr, 10 k.y., and 10m.y. time scales. *Geology* 29 (7), 591–594. [https://doi.org/10.1130/0091-7613\(2001\)029<0591:Meoyky>2.0.Co;2](https://doi.org/10.1130/0091-7613(2001)029<0591:Meoyky>2.0.Co;2).
- Krautblatter, M., Funk, D., Günzel, F.K., 2013. Why permafrost rocks become unstable: a rock-ice-mechanical model in time and space. *Earth Surf. Processes Landforms* 38 (8), 876–887. <https://doi.org/10.1002/esp.3374>.
- Krautblatter, M., Verleysdonk, S., Flores-Orozco, A., Kemna, A., 2010. Temperature-calibrated imaging of seasonal changes in permafrost rock walls by quantitative electrical resistivity tomography (Zugspitze, German/Austrian Alps). *J. Geophys. Res.* 115, F02003. <https://doi.org/10.1029/2008JF001209>.
- Leith, K., Moore, J.R., Amann, F., Loew, S., 2014. Subglacial extensional fracture development and implications for Alpine Valley evolution. *J. Geophys. Res.-Earth Surf.* 119 (1), 62–81. <https://doi.org/10.1002/2012jf002691>.
- Lifton, N., Sato, T., Dunai, T.J., 2014. Scaling in situ cosmogenic nuclide production rates using analytical approximations to atmospheric cosmic-ray fluxes. *Earth Planet. Sci. Lett.* 386, 149–160. <https://doi.org/10.1016/j.epsl.2013.10.052>.
- Luetsch, M., Lehning, M., Haeberli, W., 2008. A sensitivity study of factors influencing warm/thin permafrost in the Swiss Alps. *J. Glaciol.* 54 (187), 696–704. <https://doi.org/10.3189/002214308786570881>.
- Magnin, F., Eitzel, B., Westermann, S., Isaksen, K., Hilger, P., Hermanns, R.L., 2019. Permafrost distribution in steep rock slopes in Norway: measurements, statistical modelling and implications for geomorphological processes. *Earth Surf. Dyn.* 7 (4), 1019–1040. <https://doi.org/10.5194/esurf-7-1019-2019>.
- Matthews, J.A., Winkler, S., Wilson, P., Tomkins, M.D., Dortch, J.M., Mounre, R.W., Hill, J.L., Owen, G., Vater, A.E., 2018. Small rock-slope failures conditioned by Holocene permafrost degradation: a new approach and conceptual model based on Schmidt-hammer exposure-age dating, Jotunheimen, southern Norway. *Boreas* 47 (4), 1144–1169. <https://doi.org/10.1111/bor.12336>.
- McColl, S.T., 2012. Paraglacial rock-slope stability. *Geomorphology* 153–154, 1–16. <https://doi.org/10.1016/j.geomorph.2012.02.015>.
- McColl, S.T., Draebing, D., 2019. Rock slope instability in the proglacial zone: state of the Art. In: Heckmann, T., Morche, D. (Eds.), *Geomorphology of Proglacial Systems - Landform and Sediment Dynamics in Recently Deglaciated Alpine Landscapes*. Springer, Heidelberg, pp. 119–141. https://doi.org/10.1007/978-3-319-94184-4_8.
- MeteoSwiss, 2022a. Climate data station Fahey 1981-2019. Provided by MeteoSwiss, the Swiss Federal Office of Meteorology and Climatology.
- MeteoSwiss, 2022b. Climate data station Grächen, 1864-2019. Provided by MeteoSwiss, the Swiss Federal Office of Meteorology and Climatology.
- MeteoSwiss, 2022c. Climate data station Oberer Stelligletscher 2000-2019. Provided by MeteoSwiss, the Swiss Federal Office of Meteorology and Climatology.
- Mohadjer, S., Ehlers, T.A., Nettesheim, M., Ott, M.B., Glatz, C., Drews, R., 2020. Temporal variations in rockfall and rock-wall retreat rates in a deglaciated valley over the past 11 k.y. *Geology* 48 (6), 594–598. <https://doi.org/10.1130/g47092.1>.
- Noetzi, J., Gruber, S., Kohl, T., Salzmann, T., Haeberli, W., 2007. Three-dimensional distribution and evolution of permafrost temperatures in idealized high-mountain topography. *J. Geophys. Res. - Earth Surf.* 112, F02S13. <https://doi.org/10.1029/2006JF000545>.
- Oswald, P., Strasser, M., Hammerl, C., Moernaut, J., 2021. Seismic control of large prehistoric rockslides in the Eastern Alps. *Nat. Commun.* 12 (1), 1059. <https://doi.org/10.1038/s41467-021-21327-9>.
- Otto, J.C., Sass, O., 2006. Comparing geophysical methods for talus slope investigations in the Turtmann valley (Swiss Alps). *Geomorphology* 76 (3–4), 257–272. <https://doi.org/10.1016/j.geomorph.2005.11.008>.
- Otto, J.C., Schrott, L., Jaboyedoff, M., Dikau, R., 2009. Quantifying sediment storage in a high alpine valley (Turtmann, Switzerland). *Earth Surf. Processes Landforms* 34 (13), 1726–1742. <https://doi.org/10.1002/esp.1856>.
- Phillips, M., Wolter, A., Lüthi, R., Amann, F., Kenner, R., Bühler, Y., 2016. Rock slope failure in a recently deglaciated permafrost rock wall at Piz Kesch (Eastern Swiss Alps), February 2014. *Earth Surf. Process. Landforms* 42 (3), 426–438. <https://doi.org/10.1002/esp.3992>.
- Ravanel, L., Deline, P., 2010. Climate influence on rockfalls in high-Alpine steep rockwalls: the north side of the Aiguilles de Chamonix (Mont Blanc massif) since the end of the "Little Ice Age". *Holocene* 21 (2), 357–365. <https://doi.org/10.1177/0959683610374887>.
- Ravanel, L., Magnin, F., Deline, P., 2017. Impacts of the 2003 and 2015 summer heatwaves on permafrost-affected rock-walls in the Mont Blanc massif. *Sci. Total Environ.* 609, 132–143. <https://doi.org/10.1016/j.scitotenv.2017.07.055>.
- Rempel, A.W., Marshall, J.A., Roering, J.J., 2016. Modeling relative frost weathering rates at geomorphic scales. *Earth Planet. Sci. Lett.* 453, 87–95. <https://doi.org/10.1016/j.epsl.2016.08.019>.
- Sadler, P.M., 1981. Sediment accumulation rates and the completeness of stratigraphic sections. *J. Geol.* 89 (5), 569–584. <https://doi.org/10.1086/628623>.
- Samartin, S., Heiri, O., Joos, F., Renssen, H., Franke, J., Brönnimann, S., Tinner, W., 2017. Warm Mediterranean mid-Holocene summers inferred from fossil midge assemblages. *Nat. Geosci.* 10 (3), 207–212. <https://doi.org/10.1038/ngeo2891>.
- Sass, O., 2005. Spatial patterns of rockfall intensity in the northern Alps. *Zeitschrift für Geomorphologie, Supplementary Issues* 138, 51–65.
- Sass, O., 2007. Bedrock detection and talus thickness assessment in the European Alps using geophysical methods. *J. Appl. Geophys.* 62 (3), 254–269. <https://doi.org/10.1016/j.jappgeo.2006.12.003>.
- Sass, O., Wollny, K., 2001. Investigations regarding Alpine talus slopes using ground-penetrating radar (GPR) in the Bavarian Alps, Germany. *Earth Surf. Processes and Landforms* 26 (10), 1071–1086. <https://doi.org/10.1002/esp.254>.
- Savi, S., Comiti, F., Strecker, M.R., 2021. Pronounced increase in slope instability linked to global warming: a case study from the Eastern European Alps. *Earth Surf. Process. Landforms* 46 (7), 1328–1347. <https://doi.org/10.1002/esp.5100>.
- Savi, S., Delunel, R., Schlunegger, F., 2015. Efficiency of frost-cracking processes through space and time: an example from the eastern Italian Alps. *Geomorphology* 232, 248–260. <https://doi.org/10.1016/j.geomorph.2015.01.009>.
- Scapozza, C., Baron, L., Lambiel, C., 2015. Borehole Logging in Alpine Periglacial Talus Slopes (Valais, Swiss Alps). *Permafrost Periglac. Process.* 26 (1), 67–83. <https://doi.org/10.1002/ppp.1832>.
- Schenk, F., Väiliranta, M., Muschitiello, F., Tarasov, L., Heikkilä, M., Björck, S., Brandefelt, J., Johansson, A.V., Näslund, J.-O., Wohlfarth, B., 2018. Warm summers

- during the Younger Dryas cold reversal. *Nat. Commun.* 9 (1), 1634. <https://doi.org/10.1038/s41467-018-04071-5>.
- Schimmelpfennig, I., Schaefer, J.M., Akçar, N., Ivy-Ochs, S., Finkel, R.C., Schlüchter, C., 2012. Holocene glacier culminations in the Western Alps and their hemispheric relevance. *Geology* 40 (10), 891–894. <https://doi.org/10.1130/g33169.1>.
- Schindelwig, I., Akçar, N., Kubik, P.W., Schlüchter, C., 2012. Lateglacial and early Holocene dynamics of adjacent valley glaciers in the Western Swiss Alps. *J. Quat. Sci.* 27 (1), 114–124. <https://doi.org/10.1002/jqs.1523>.
- Swissair Photo, A.G., 1964. Turtmanntal, Barrhorn. ETH-Bibliothek Zürich. <https://doi.org/10.3932/ethz-a-000304060>.
- Verdian, J.P., Sklar, L.S., Riebe, C.S., Moore, J.R., 2021. Sediment size on talus slopes correlates with fracture spacing on bedrock cliffs: implications for predicting initial sediment size distributions on hillslopes. *Earth Surf. Dynam.* 9 (4), 1073–1090. <https://doi.org/10.5194/esurf-9-1073-2021>.
- Wegmann, M., Gudmundsson, G.H., Haerberli, W., 1998. Permafrost Changes in Rock Walls and the retreat of alpine glaciers: a Thermal Modelling Approach. *Permafrost Periglac. Process.* 9, 23–33. [https://doi.org/10.1002/\(SICI\)1099-1530\(199801/03\)9:1<23::AID-PPP274>3.0.CO;2-Y](https://doi.org/10.1002/(SICI)1099-1530(199801/03)9:1<23::AID-PPP274>3.0.CO;2-Y).
- Williams, J.G., Rosser, N.J., Hardy, R.J., Brain, M.J., 2019. The importance of monitoring interval for rockfall magnitude-frequency estimation. *J. Geophys. Res.* 124 (12), 2841–2853. <https://doi.org/10.1029/2019jf005225>.